

Signatures of vector-like top partners decaying into new neutral scalar or pseudoscalar bosons

R. Benbrik,^a E. Bergeaas Kuutmann,^{b,1} D. Buarque Franzosi,^c V. Ellajosyula,^b
R. Enberg,^b G. Ferretti,^c M. Isacson,^b Y.-B. Liu,^{d,2} T. Mandal,^b T. Mathisen,^b
S. Moretti,^{e,3} L. Panizzi.^{b,2}

^a*Cadi Ayyad University, Marrakesh, Morocco*

^b*Uppsala University, Uppsala, Sweden*

^c*Chalmers University of Technology, Göteborg, Sweden*

^d*Henan Institute of Science and Technology, Xinxiang, P.R.China*

^e*University of Southampton, Southampton, UK*

E-mail: elin.bergeaas.kuutmann@physics.uu.se

ABSTRACT: We explore the phenomenology of models containing one Vector-Like Quark (VLQ), t' , which can decay into the Standard Model (SM) top quark, t , and a new spin-0 neutral boson, S , the latter being either a scalar or pseudoscalar state. We parametrise the underlying interactions in terms of a simplified model which enables us to capture possible Beyond the SM (BSM) scenarios. We discuss in particular three such scenarios: one where the SM state is supplemented by an additional scalar, one which builds upon a 2-Higgs Doublet Model (2HDM) framework and another which realises a Composite Higgs Model (CHM) through partial compositeness. Such exotic decays of the t' can be competitive with decays into SM particles, leading to new possible discovery channels at the Large Hadron Collider (LHC). Assuming t' pair production via strong interactions, we design signal regions optimised for one $t' \rightarrow S t$ transition (while being inclusive on the other \bar{t}' decay, and vice versa), followed by the decay of S into the two very clean experimental signatures $S \rightarrow \gamma \gamma$ and $S \rightarrow Z(\rightarrow \ell^+ \ell^-) \gamma$. We perform a dedicated signal-to-background analysis in both channels, by using Monte Carlo (MC) event simulations modelling the dynamics from the proton-proton to the detector level. Under the assumption of $\text{BR}(t' \rightarrow S t) = 100\%$, we are therefore able to realistically quantify the sensitivity of the LHC to both the t' and S masses, assuming both current and foreseen luminosities. This approach paves the way for the LHC experiments to surpass current VLQ search strategies based solely on t' decays into SM bosons (W^\pm, Z, h).

¹Corresponding author.

²Also at University of Southampton.

³Also at Uppsala University.

Contents

| | | |
|----------|---|-----------|
| 1 | Introduction | 1 |
| 2 | The simplified model | 3 |
| 2.1 | Example 1: adding a VLQ and a scalar to the SM | 4 |
| 2.2 | Example 2: adding a VLQ to the 2HDM | 7 |
| 2.3 | Example 3: realisation in partial compositeness | 8 |
| 3 | LHC constraints from $\gamma\gamma$ and $Z\gamma$ resonance searches | 10 |
| 4 | Analysis | 12 |
| 4.1 | Object definition | 12 |
| 4.2 | Simulations | 14 |
| 4.3 | $S \rightarrow \gamma\gamma$ signal region | 18 |
| 4.4 | $S \rightarrow Z\gamma$ signal region | 20 |
| 4.5 | Efficiencies | 22 |
| 5 | Results | 22 |
| 5.1 | Model interpretation | 24 |
| 6 | Conclusions | 27 |
| A | Details of the models | 30 |
| A.1 | The 2HDM with an additional VLQ | 30 |
| A.2 | The composite Higgs model | 32 |
| B | Range of validity of the analysis | 36 |
| B.1 | Distinguishing the dominant chirality of t' coupling and the scalar or pseudoscalar nature of S | 36 |
| B.2 | Validity of the narrow-width approximation | 39 |
| C | Signal efficiencies | 42 |

1 Introduction

During Run II at the LHC, the ATLAS and CMS experiments have collected almost 150 fb^{-1} and 180 fb^{-1} of data, respectively, at a centre-of-mass (CM) energy of 13 TeV. These data are now being analysed by the collaborations and, so far, no significant deviations from the SM have been recorded. This has significantly restricted the parameter space of the most common scenarios attempting to solve the hierarchy problem of the SM, such as

supersymmetry and compositeness. Yet, it is important to find a viable solution to this flaw of the SM. This is inevitably connected to studying both top quark and Higgs boson dynamics, as the hierarchy problem of the SM originates from their mutual interactions. A pragmatic approach is to investigate BSM scenarios in which either of or both the top and Higgs sectors of the SM are enlarged through the presence of companions to the SM states (t and h), by which we mean additional spin-1/2 and spin-0 states, respectively, with the same electromagnetic (EM) charge but different mass (naturally heavier) and possibly different quantum numbers as well.

Some guidance in exploring the various BSM possibilities in this respect is afforded by experimental measurements of observables where both the top quark and the SM-like Higgs boson enter. On the one hand, a sequential fourth family of chiral SM quarks is strongly constrained indirectly from Higgs boson measurements due to their non-decoupling properties [1], while VLQs (which transform as triplets under colour but whose left- and right-handed components have identical electroweak (EW) quantum numbers) can evade these bounds easily. On the other hand, the possibility of the existence of additional Higgs bosons has not been excluded by experimental data and may well be theoretically motivated by the fact that neither the matter nor the gauge sectors are minimal. Moreover, the Higgs sector is extended in any supersymmetric model or in the 2HDM.

Similarly, any model in which a Higgs boson arises as a pseudo-Nambu-Goldstone Boson (pNGB), other than the minimal model based on the symmetry breaking pattern $SO(5)/SO(4)$, will include additional light (pseudo)scalars that might well have eluded direct searches due to their reduced couplings to the EW bosons and top quark.

Hence, it is of some relevance to assess the viability at the LHC of BSM models with both top quark partners (of VLQ nature) and companion scalar or pseudoscalar particles (both charged and neutral). In fact, it is particularly intriguing to investigate the possibility of isolating experimental signatures where the two particle species interact with each other, namely, when the t' decays into a new (pseudo)scalar.

So far, collider searches for a VLQ companion to the SM top quark [2, 3] have mostly been carried out under the assumption that it decays exclusively into SM particles, namely, a heavy quark (b, t) and a boson (W^\pm, Z, h), compatibly with the EM charge assignments. Specifically, for the case of a top-like VLQ, t' , the decays considered are $t' \rightarrow Zt$, $t' \rightarrow ht$ and $t' \rightarrow W^+b$, with varying branching ratios (BRs) adding up to 100%, see e.g. [4–13].

It is thus important to ask how the presence of exotic decay channels of VLQs can affect the current bounds and whether these might actually be promising discovery channels on their own. This question has been asked in similar contexts in various preceding works [14–20], each concentrating on a specific BSM construction. Here, in contrast, we follow the approach of [21], which adopts a set of simplified scenarios based on effective Lagrangians (motivated by compositeness).

In our paper, we build upon this last work, by adopting a simplified scenario which contains, above and beyond the SM particle spectrum, a top-like VLQ, t' , as well as an additional scalar (or pseudoscalar) particle, S , in turn leading to the new decay channel $t' \rightarrow St$. As for the decay modes of S , we will concentrate on two of the experimentally cleanest channels accessible at the LHC, namely, $S \rightarrow \gamma\gamma$ and $S \rightarrow Z\gamma$, with the Z

boson decaying in turn into electrons or muons. We will show in section 2 that there exist well motivated phenomenological scenarios where these can indeed be decay modes with significant BRs, for the case of both fundamental and composite Higgs states. In section 3 we estimate LHC constraints using published ATLAS and CMS searches in $\gamma\gamma$ and $Z\gamma$ final states while in section 4 we will describe our MC simulations, based on the pair production process $pp \rightarrow t'\bar{t}'$, followed by the decay chains $t' \rightarrow S(\rightarrow \gamma\gamma)t$ or $t' \rightarrow S(\rightarrow Z\gamma)t$, with the \bar{t}' treated inclusively (and vice versa). Section 5 is then dedicated to interpreting the ensuing MC results in three theoretical scenarios embedding a t' alongside additional (pseudo)scalar states focusing on cases with $\text{BR}(t' \rightarrow St) = 100\%$, while in section 6 we conclude.

2 The simplified model

The purpose of this section is to present the relevant details about the class of models whose phenomenology we aim to study. We begin with a general description of a simplified model that captures all relevant features. This is the model used for the analysis in section 4. We then justify the use of this simplified model by introducing three more specific models that can all be described with the same generic Lagrangian by a mapping of the fields and the couplings, provided that the processes considered in this paper are studied.

As discussed in the introduction, we are interested in exotic decays of a top partner t' (of mass $m_{t'}$) into the ordinary top quark t and a scalar (or pseudoscalar) generically denoted by S (of mass m_S) in the simplified model. We can thus augment the SM Lagrangian \mathcal{L}_{SM} by the following interaction Lagrangian with operators up to dimension five involving these two additional fields,

$$\begin{aligned} \mathcal{L}_{\text{BSM}} = & \kappa_L^S \bar{t}'_R t_L S + \kappa_R^S \bar{t}'_L t_R S + \text{h.c.} \\ & - \frac{S}{v} \sum_f m_f (\kappa_f \bar{f} f + i \tilde{\kappa}_f \bar{f} \gamma_5 f) + \frac{S}{v} (2\lambda_W m_W^2 W_\mu^+ W^{-\mu} + \lambda_Z m_Z^2 Z_\mu Z^\mu) \\ & + \frac{S}{16\pi^2 v} \sum_V \left(\kappa_V g_V^2 V_{\mu\nu}^a V^{a\mu\nu} + \tilde{\kappa}_V g_V^2 V_{\mu\nu}^a \tilde{V}^{a\mu\nu} \right). \end{aligned} \quad (2.1)$$

Here κ_L^S and κ_R^S are the Yukawa couplings of the S to the t and t' . In the second line, f sums over all SM fermions (including the top t) and κ_f is the dimensionless reduced Yukawa coupling. In the last line $V_{\mu\nu}$ denotes the field strengths of the $U(1)_Y$, $SU(2)_L$ and $SU(3)_C$ gauge bosons B_μ, W_μ, G_μ in the gauge eigenbasis, g_V is the associated gauge coupling (g', g, g_s respectively) and $\tilde{V}_{\mu\nu} = (1/2)\epsilon_{\mu\nu\rho\gamma} V^{\rho\gamma}$ is the dual field strength tensor. The coefficients $\tilde{\kappa}_V$ and κ_V are couplings associated with dimension-five operators and are typically generated by loops of heavy particles or via anomalies. The couplings λ_V for any gauge boson V are only generated if S is charged under some of the SM gauge groups and gets a vacuum expectation value (VEV) or if it mixes with such states, e.g., the Higgs boson. Since $SU(3)_C$ and $U(1)_{\text{EM}}$ are unbroken for the strong and EM interactions, $\lambda_V = 0$ for the respective gauge bosons. We choose to normalise all terms with only one dimensionful parameter, the VEV $v = 246 \text{ GeV}$.

In practice, we consider an S state of either scalar or pseudoscalar nature, but not a mixture. We therefore do not consider CP-violation in this paper. This means that either $\tilde{\kappa}_V$ or $\tilde{\kappa}_f$ are zero, in the scalar case, or κ_V , λ_V and κ_f are zero, in the pseudoscalar case.

The total widths of t' and S are kept as free parameters in the simulation as an indication that other interactions and other states might be present. These interactions are not explicitly required to describe the process $pp \rightarrow t' \bar{t}' \rightarrow SSt\bar{t}$ apart from their contribution to the total widths. Here we only report the analytic expression for the partial width of the exotic t' decay, specifically.

$$\Gamma_{t' \rightarrow St} = \frac{1}{32\pi} m_{t'} \left[(1 + x_t^2 - x_S^2) (|\kappa_L^S|^2 + |\kappa_R^S|^2) + 4x_t (\text{Re } \kappa_L^S \text{Re } \kappa_R^S + \text{Im } \kappa_L^S \text{Im } \kappa_R^S) \right] \\ \times (1 + x_t^4 + x_S^4 - 2x_t^2 - 2x_S^2 - 2x_t^2 x_S^2)^{\frac{1}{2}}, \quad (2.2)$$

where $x_t \equiv m_t/m_{t'}$ and $x_S \equiv m_S/m_{t'}$. This formula is valid for decays into both scalar and pseudoscalar S .

This defines the simplified model that will be used in the rest of this paper. Let us now briefly discuss three specific examples of models that motivate the use of the above simplified model and the mapping between the former and the latter. The results in this paper, given in terms of the simplified model above, can then easily be reinterpreted in terms of each model, if needed. In a forthcoming paper, we will specify these models in more detail and will discuss their specific phenomenology.

2.1 Example 1: adding a VLQ and a scalar to the SM

In order to illustrate how a particular model can be related to the phenomenological simplified model (eq. (2.1)), we will first present a simple model of top-quark partial compositeness (PC) in some detail. The model consists of the SM extended by a top partner VLQ and a scalar singlet. In this model the top quark acquires its mass via the mixing with the top partner. This model is not intended as a complete, realistic model, but provides an example of a model with an additional scalar S that is neutral under the SM gauge group. We will only be concerned with the couplings between the top quarks and S , leaving the coupling inducing the decay of the S to SM states as in eq. (2.1).

We denote the gauge eigenstates in the top sector by \tilde{t}_L , \tilde{t}_R and T . The notation $\tilde{t}_{L/R}$ is to prevent confusion with the mass eigenstates that are to be denoted by t and t' . The Lagrangian for this model before EW symmetry breaking (EWSB) can be written as

$$\mathcal{L}_{\text{kin}} \supset \bar{T} (i\not{D} - M) T + \frac{1}{2} (\partial_\mu S) (\partial^\mu S) - \frac{1}{2} m_S^2 S^2, \quad (2.3)$$

$$\mathcal{L}_{\text{int}} \supset -\lambda_S^a S \bar{T}_L T_R - \lambda_S^b S \bar{T}_L \tilde{t}_R - \tilde{y} (\bar{Q}_L \tilde{H}) \tilde{t}_R - \lambda_1 (\bar{Q}_L \tilde{H}) T_R - m_2 \bar{T}_L \tilde{t}_R + \text{h.c.}, \quad (2.4)$$

where the SM Higgs doublet is denoted by H with $\tilde{H} = i\sigma_2 H^*$. The SM Yukawa coupling for the top quark is here denoted by \tilde{y} and Q_L is the left-handed quark doublet of the third generation. The couplings $\lambda_S^{a,b}$ are real if S is a scalar and purely imaginary if S is a

pseudoscalar. The mass m_2 is a non-diagonal entry in the mass matrix of eq. (2.5). The remaining couplings are dimensionless. After EWSB, we have a mass matrix

$$\mathcal{L}_t \supset (\tilde{t}_L \bar{T}_L) \begin{pmatrix} m_{\tilde{t}} & m_1 \\ m_2 & M \end{pmatrix} \begin{pmatrix} \tilde{t}_R \\ T_R \end{pmatrix} + \text{h.c.}, \quad (2.5)$$

where we defined $m_{\tilde{t}} = \tilde{y}v/\sqrt{2}$ and $m_1 = \lambda_1 v/\sqrt{2}$. The mass matrix can be diagonalised by bi-orthogonal rotations by the angles $\theta_{L,R}$, separately for left- and right-handed fermions, as follows (where $s_X \equiv \sin \theta_X$ and $c_X \equiv \cos \theta_X$)

$$\begin{pmatrix} t_{L,R} \\ t'_{L,R} \end{pmatrix} = \begin{pmatrix} c_{L,R} & -s_{L,R} \\ s_{L,R} & c_{L,R} \end{pmatrix} \begin{pmatrix} \tilde{t}_{L,R} \\ T_{L,R} \end{pmatrix}, \quad (2.6)$$

where $\{t, t'\}$ are the mass eigenstates and the mixing angles are given by

$$\tan(2\theta_L) = \frac{2(m_{\tilde{t}}m_2 + Mm_1)}{M^2 - m_{\tilde{t}}^2 - m_1^2 + m_2^2}, \quad \tan(2\theta_R) = \frac{2(m_{\tilde{t}}m_1 + Mm_2)}{M^2 - m_{\tilde{t}}^2 + m_1^2 - m_2^2}. \quad (2.7)$$

The mass eigenvalues m_t and $m_{t'}$ are found by computing the eigenvalues. This model can be mapped to the simplified model Lagrangian in eq. (2.1) by performing the rotation in eq. (2.6) inside eq. (2.4). Focusing on the mixing terms yields

$$\kappa_L^S = \left(\lambda_S^a s_L c_R + \lambda_S^b s_L s_R \right)^*, \quad \kappa_R^S = \lambda_S^a c_L s_R - \lambda_S^b c_L c_R, \quad (2.8)$$

while for the coupling to the top we have

$$\kappa_t = \text{Re} \left(-\lambda_S^a s_L s_R + \lambda_S^b s_L c_R \right), \quad \tilde{\kappa}_t = \text{Im} \left(-\lambda_S^a s_L s_R + \lambda_S^b s_L c_R \right). \quad (2.9)$$

There is also a diagonal term involving the t' , which is proportional to $\lambda_S^a c_L c_R + \lambda_S^b c_L s_R$. It is not included in the simplified model, but instead generates a contribution to the effective coefficients κ_V and $\tilde{\kappa}_V$ from loop diagrams.

Let us also briefly discuss the decays of the t' and S in this model. The t' has both the standard and non-standard decay channels discussed above, where the width of the $t' \rightarrow S t$ channel is given by eq. (2.2) with the couplings defined in eq. (2.8). The scalar can, in general, decay into the final states $gg, \gamma\gamma, Z\gamma, ZZ, WW$ and $t\bar{t}$. We always assume $m_S < m_{t'}$, which forbids the decay $S \rightarrow t'\bar{t}'$. Apart from the $t\bar{t}$ channel, all the other decays are generated by loops of the t and t' .

We may now examine the decay of the t' and S depending on the coupling of T_L with T_R and \tilde{t}_R . The $t' \rightarrow S t$ decay is induced by the λ_S^a and λ_S^b couplings. If we are interested in a large $\text{BR}_{t' \rightarrow St}$, we may achieve that easily in a wide region of parameter space by considering suitable values of these couplings. For example, when the T_L couples to \tilde{t}_R (i.e., $\lambda_S^a = 0, \lambda_S^b \neq 0$), a small λ_S^b can induce large $\text{BR}_{t' \rightarrow St}$ as the λ_S^b part of κ_R^S in eq. (2.8) is proportional to $c_L c_R \sim 1$. If the T_L only couples to T_R (i.e., $\lambda_S^a \neq 0, \lambda_S^b = 0$), a large $\text{BR}_{t' \rightarrow St}$ is realised when λ_S^a is sufficiently large, as the partial width is proportional to $(\lambda_S^a/\lambda_t)^2$. However, this will also increase the s -channel production of S through gg fusion,

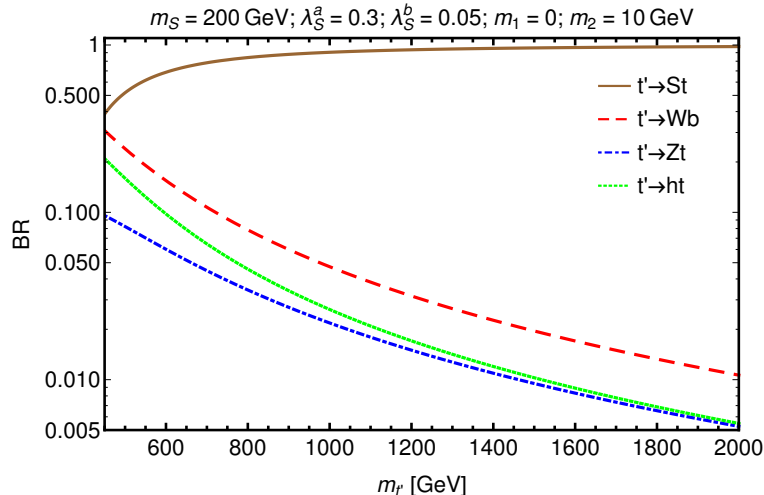


Figure 1: BRs of t' as a function of the mass for a specific parameter point.

therefore, this scenario is heavily constrained by the $gg \rightarrow S \rightarrow \gamma\gamma$ resonance search data from the LHC. In figure 1, we show the BRs of t' for a specific benchmark point where the $t' \rightarrow St$ channel has a BR of almost 100%.

As for the S decay, the $S \rightarrow gg$ channel dominates if the $t\bar{t}$ decay is not kinematically allowed. The total decay width is governed by $\Gamma_{S \rightarrow gg}$, and hence the branching ratio in the $\gamma\gamma$ channel is approximately

$$\text{BR}_{S \rightarrow \gamma\gamma} \simeq \frac{\Gamma_{S \rightarrow \gamma\gamma}}{\Gamma_{S \rightarrow gg}} = \frac{8\alpha_{EM}^2}{9\alpha_S^2} \approx 0.004. \quad (2.10)$$

Note that this equation is only valid in the model discussed in this section. The general formula for the ratio in eq. (2.10) in the simplified model in eq. (2.1) is given by

$$\frac{\Gamma_{S \rightarrow \gamma\gamma}}{\Gamma_{S \rightarrow gg}} = \frac{\alpha_{EM}^2 (\kappa_B + \kappa_W)^2}{8\alpha_S^2 \kappa_g^2}. \quad (2.11)$$

Other loop induced channels are even more suppressed than $S \rightarrow \gamma\gamma$. For example, the partial widths of $S \rightarrow Z\gamma$ and $S \rightarrow ZZ$, modulo negligible m_Z corrections, are $2 \tan^2 \theta_W \Gamma_{S \rightarrow \gamma\gamma}$ and $\tan^4 \theta_W \Gamma_{S \rightarrow \gamma\gamma}$ respectively. Usually, if $m_S > 2m_t$, the tree-level $t\bar{t}$ channel totally dominates the loop induced decays. However, in a region of parameter space, the $t\bar{t}$ decay can be tuned down by suitable values of the off-diagonal entries in the mass matrix in eq. (2.5). We find that when $\sin \theta_L \ll \sin \theta_R$ (or equivalently $m_1 \ll m_2$), the effective $St\bar{t}$ coupling, depending on the λ_S^a and λ_S^b couplings, is not sufficiently large to compete with the loop induced decays of S . Note that the $\gamma\gamma$ channel could in principle be increased in an extended model by introducing new fields that couple to photons but not to gluons, e.g., charged scalars, new colour singlet charged gauge bosons, vector-like leptons, etc. Moreover, the partial width depends on the SU(2) representation of t' as well as S .

2.2 Example 2: adding a VLQ to the 2HDM

The 2HDM (see [22] for a review) is widely used as a minimal model for an extended Higgs sector that goes beyond additional singlet scalars. With additional vector-like top partners (see [23–25] for previous work), the 2HDM may be seen as the low-energy manifestation of a composite Higgs scenario, such as in [26]. Specifically, we here consider a vector-like top partner T with charge $+2/3$ in the singlet representation of the SM EW group. We further consider Yukawa couplings of the SM quarks of Type-II, i.e., that the up- and down-type quarks couple to different doublets.

The scalar sector of the 2HDM has an additional neutral scalar H , a pseudoscalar A and a charged H^\pm state. This enables us to obtain simple formulas where either H or A can play the role of S in the simplified model Lagrangian in eq. (2.1). The details of the model and the involved parameters, as well as the mapping to the simplified model Lagrangian of eq. (2.1) are discussed in appendix A.1. Let us here only discuss the mixing of the physical top quark t and top partner t' .

The physical mass of the heavy top, $m_{t'}$, is different from the mass M of the vector-like T due to t - T mixing. The mass matrix can be diagonalised in the same way as in eq. (2.6) to obtain the physical states $(t_{L,R}, t'_{L,R})$ in terms of the gauge eigenstates $(\tilde{t}_{L,R}, T_{L,R})$. The mixing angles θ_L and θ_R are not independent parameters and we can derive similar relations to eq. (2.6) (see eq. (A.7)), in terms of the Yukawa couplings y_t and ξ_T that couple the left-handed quark doublet Q_L to the right-handed SM top \tilde{t}_R and the vector-like T_R , respectively (see eq. (A.4) and eq. (A.14)). The two mixing angles in this case satisfy [25]

$$\tan \theta_L = \frac{m_t}{m_{t'}} \tan \theta_R, \quad \frac{\xi_T}{y_t} = s_L c_L \frac{m_{t'}^2 - m_t^2}{m_t m_{t'}}, \quad (2.12)$$

while the mass of the t' is related to the Lagrangian parameters and the physical top quark mass via

$$m_{t'}^2 = M^2 \left(1 + \frac{\xi_T^2 v^2}{2(M^2 - m_t^2)} \right). \quad (2.13)$$

The t' - t interaction can thus be described by three independent physical parameters: two quark masses m_t , $m_{t'}$, and a mixing angle, $s_L = \sin \theta_L$.

In the 2HDM with VLQ, the scalar S is an additional Higgs boson. The dimension-five operators in eq. (2.1) are then generated through loops, and in general S can be produced through $gg \rightarrow S$. It can in general decay in all the bosonic channels that we consider in this paper and, in addition, in fermionic channels. The branching ratios in this model are discussed in section 5. These channels give rise to constraints from all the usual collider observables. In addition, the scalar sector of this model is subject to the same unitarity, perturbativity and vacuum stability constraints as the usual 2HDM [22, 27]. The Yukawa coupling y_t is constrained from unitarity to be less than 4π , while ξ_T is a derived quantity. Since the new top partner will contribute to gauge boson self energies, the mixing angle θ_L can be constrained from EW Precision Tests (EWPTs) such as the S and T parameters.

2.3 Example 3: realisation in partial compositeness

Lastly, we present a Composite Higgs Model (CHM), which motivates the analysis in this paper by having a top partner with enhanced exotic decay mode and a pseudoscalar with dominant $Z\gamma$ decay. The model is closely related to one of the earliest non-minimal models of composite Higgs with fermionic partial compositeness [28], based on the coset space $SU(4)/Sp(4)$, where Sp is the symplectic group. The usual Higgs field \mathcal{H} is a bi-doublet of $SU(2)_L \times SU(2)_R$, which together with a singlet S (usually denoted by η in the CHM literature) forms the five dimensional anti-symmetric irreducible representation of $Sp(4)$,

$$\mathcal{H} \oplus S \equiv \begin{pmatrix} H^{0*} & H^+ \\ -H^{+*} & H^0 \end{pmatrix} \oplus S \in (\mathbf{2}, \mathbf{2}) \oplus (\mathbf{1}, \mathbf{1}) = \mathbf{5}. \quad (2.14)$$

This scenario has the further appeal of belonging to a class of models that can be obtained from an underlying gauge theory with fermionic matter [29, 30] and the additional features arising from this fact have been studied in, e.g., [31]. Here, however, we want to focus on the bare bones of the model, namely the above-mentioned coset structure with the addition of one fermionic partner Ψ . (We only consider partial compositeness in the top sector).

The fermionic sector also consists of a bi-doublet and a singlet in the $\mathbf{5}$ of $Sp(4)$. We will see that, as already anticipated in [21] (see also [14]), the possible decay patterns of the fermionic partners are richer than what is usually considered in current searches and, in particular, the lightest top-partner has an enhanced decay into the exotic channel $t' \rightarrow St$.

To summarise, in addition to the SM fields the model has an additional pseudoscalar S , three top partners T, T', \tilde{T} (all of electric charge $+2/3$), a bottom partner B (charge $-1/3$) and an additional coloured fermion X of charge $+5/3$. Like in the previous example models, all of these fermions are vector-like Dirac spinors, to be thought of as in the gauge eigenbasis, i.e., before their mass matrices are diagonalised. The difference here is that there are more than one new fermion.

The mixing with the third family quarks of the SM depends on how they are embedded in a representation of $SU(4)$. We choose this embedding such that the custodial symmetry of [32] is preserved, see appendix A.2 for details. In addition, the choice of having an elementary \tilde{t}_R distinguishes this model from similar ones studied in [33], where the \tilde{t}_R was taken to be fully composite. The elementary \tilde{t}_R seems more appealing, since chiral fermions are notoriously difficult to obtain from underlying strongly coupled theories. We do not address the origin of the bottom quark mass in this work, which would add additional model dependence that is not relevant for the experimental signatures of interest. See appendix A.2 for more details on the construction of the model and the singular value decomposition of the mass matrix.

We end up with four top quark mass eigenstates, which we denote, in increasing mass order, by t, t', t'' and t''' . Here t is the known SM top quark of mass $m_t = 173$ GeV. We diagonalise the mass matrix numerically, but a perturbative expansion for the masses gives

some insight into the mass spectrum. We find (see appendix A.2)

$$m_t = \frac{y_L y_R f v}{\sqrt{2\widehat{M}}} + \mathcal{O}(v^2/f^2), \quad m_{t'} = M, \quad (2.15)$$

$$m_{t''} = M + \mathcal{O}(v^2/f^2), \quad m_{t'''} = \widehat{M} + \mathcal{O}(v^2/f^2), \quad (2.16)$$

where M is the mass parameter of the Ψ , y_L and y_R are the respective couplings of the Q_L and \tilde{t}_R to the Ψ and pNGBs while f is the ‘‘pion decay constant’’ of the strongly coupled theory. We also defined $\widehat{M} = \sqrt{M^2 + y_L^2 f^2}$. The mass of the bottom partner (mostly aligned with B) turns out to be of the same order as that of the heaviest top partner $m_{t'''}$, while X has mass equal to $M \equiv m_{t'}$ since it does not mix with anything.

Substituting the mass eigenstates (see appendix A.2) into the Lagrangian and considering the coupling that mixes the two lightest eigenstates t and t' with the pNGBs, we see that no mixing with the Higgs field h arises, while the S couples, up to terms of order $\mathcal{O}(v^2/f^2)$, as

$$\mathcal{L} = -iy_R S \tilde{t}_L t_R - \frac{iy_L v M}{\sqrt{2f\widehat{M}}} S \tilde{t}'_R t_L + \text{h.c.}, \quad (2.17)$$

allowing us to match the models with the parameters of the phenomenological Lagrangian eq. (2.1)

$$\kappa_R^S = -iy_R, \quad \kappa_L^S = -\frac{iy_L v M}{\sqrt{2f\widehat{M}}}. \quad (2.18)$$

From the analysis of the spectrum and of the couplings, we see that we can concentrate on a model with two mass degenerate VLQs t' and X , with $\sim 100\%$ branching ratios $X \rightarrow W^+ t$ and $t' \rightarrow S t$. The decay modes of t' to SM vector bosons are highly suppressed, t' being a singlet of $SU(2)_L \times SU(2)_R$. For this model, it is thus crucial to understand whether the BSM decay $t' \rightarrow S t$ can compete with the SM decay $X \rightarrow W^+ t$ whose signatures have been looked for at the LHC [6] providing bounds to the model parameter $M > 1.2 \text{ TeV}$. We address this question in this work. Just above the t' mass scale there is a further top partner, t'' , with more diverse and model dependent decay modes, so it is likely to be less relevant to experimental searches. The last top partner t''' and the B are heavy and can be ignored altogether.

The coupling of the S to gauge bosons can be motivated by the analysis of the underlying gauge theory [29, 30] and is given at leading order by the Lagrangian

$$\mathcal{L}_{SVV} = \frac{A \cos \theta}{16\pi^2 f} S \left(\frac{g^2 - g'^2}{2} Z_{\mu\nu} \tilde{Z}^{\mu\nu} + gg' F_{\mu\nu} \tilde{Z}^{\mu\nu} + g^2 W_{\mu\nu}^+ \tilde{W}^{-\mu\nu} \right), \quad (2.19)$$

where the ‘‘Abelian’’ field strength tensors are defined as $V_{\mu\nu} = \partial_\mu V_\nu - \partial_\nu V_\mu$, thus omitting the ‘‘non-Abelian’’ part, which would contribute to interactions with three and four gauge bosons that we ignore here. A is a model dependent dimensionless anomaly coefficient: $1 \lesssim A \lesssim 10$. Note that there are no couplings of type SSV since the S does not acquire a VEV. Also, there is no anomalous coupling $SF_{\mu\nu}\tilde{F}^{\mu\nu}$ to the EM field, thus the decay $S \rightarrow \gamma\gamma$ is highly suppressed and for $m_S \lesssim 2m_W$ the decay $S \rightarrow Z\gamma$ has near 100%

branching ratio. Once again, we can match the current model with the remaining couplings of the phenomenological Lagrangian in eq. (2.1):

$$\tilde{\kappa}_W = -\tilde{\kappa}_B = \frac{Av}{2f} \cos \theta. \quad (2.20)$$

The mass of S is expected to be small $m_S \sim m_h$ and thus in the region where the decay into $Z\gamma$ is motivated. It is given by $m_h/\cos\theta$ plus corrections proportional to explicit underlying fermions masses, which are disfavoured by fine tuning arguments.

As far as direct S production goes, we observe that, choosing the spurion embeddings as above, no diagonal coupling of type $S\bar{t}^i t^i$ ($t^i = t, t', t'', t'''$) is directly generated [28]. This means that the gluon fusion process is not present and the direct production proceeds mainly via EW vector bosons. Diagonal fermionic couplings for the top and for lighter fermions can be induced by further enlarging the model but we ignore them and consider the fermiophobic case. The coupling of S to fermions is nevertheless generated via loop of gauge bosons and might be relevant for low m_S [34, 35].

3 LHC constraints from $\gamma\gamma$ and $Z\gamma$ resonance searches

To perform a phenomenological analysis of the $\gamma\gamma$ and $Z\gamma$ final states it is necessary to estimate the allowed regions in the masses of the VLQ and (pseudo)scalar. This is done in this section by recasting one ATLAS and one CMS search at 13 TeV and providing the ensuing limits in the m_{ν} vs m_S plane.

The searches used for the recast are briefly described in the following.

- An ATLAS “Search for new phenomena in high-mass diphoton final states” [36], used to set constraints for the $\gamma\gamma$ final state. This search looks for resonances with spin 0 or 2 decaying into two photons. For the spin 0 resonances (of interest for our analysis) the explored diphoton invariant mass region ranges from 200 GeV to 2700 GeV. The search cuts on the transverse energy of the leading and subleading identified photons, $E_T > 40$ GeV and $E_T > 30$ GeV, respectively, and requires E_T to be larger than a fraction of the diphoton invariant mass, $E_T > 0.4m_{\gamma\gamma}$ GeV (leading photon) and $E_T > 0.3m_{\gamma\gamma}$ GeV (subleading photon).
- A CMS “Search for standard model production of four top quarks with same-sign and multilepton final states” [37], used to set constraints for the $Z\gamma$ final state. This search looks for final states with two (same-charge) or three leptons, and different numbers of jets and b -jets, depending on the signal region. No cuts are imposed on photons in the final state. The most relevant cuts are applied to the jet and b -jet multiplicity and differ depending on the signal region.

The recast simulations are done using MADGRAPH5_AMC@NLO [38] with a dedicated UFO [39] model file corresponding to the simplified Lagrangian in eq. (2.1). Events are generated at leading order and interfaced with PYTHIA 8.2 [40] and DELPHES 3 [41] for showering and fast detector simulation. As Parton Distribution Functions (PDFs), the

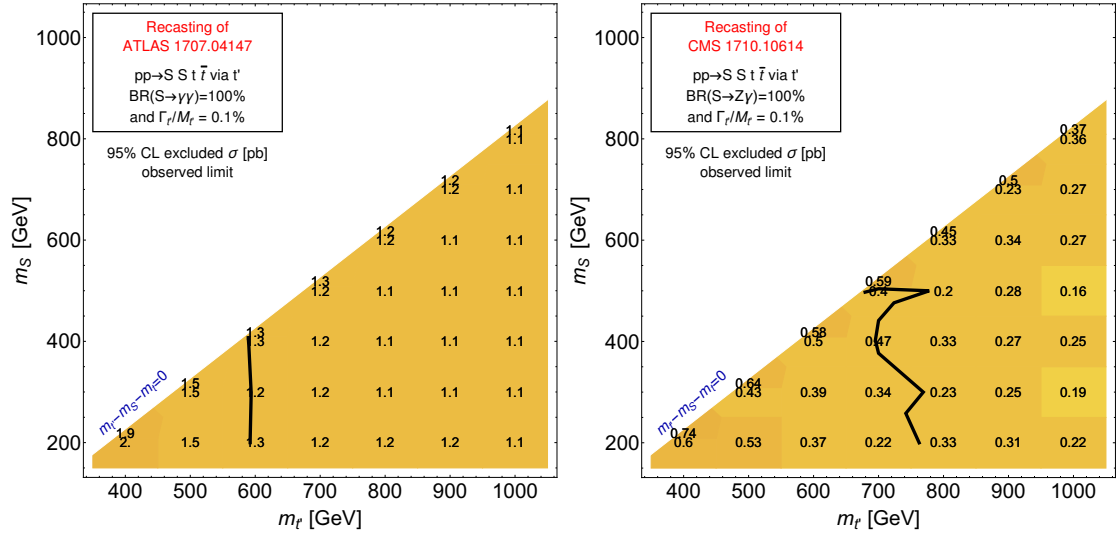


Figure 2: Upper limits on the cross section in the $m_{t'}$ vs m_S plane for the $\gamma\gamma$ (left panel) and $Z\gamma$ channels (right panel) from the recast of the ATLAS search [36] and CMS search [37], respectively. The solid black lines represents the bounds on the two masses obtained by comparing the upper limits with the pair production cross section of t' at NLO+NNLL computed through HATHOR [46] under the assumption of 100% BRs for both t' and S in the respective channels and in the narrow width approximation (NWA).

NNPDF 3.1 at NLO set [42] has been chosen, obtained through the LHAPDF 6 library [43] using PDF ID 303400. The recast and validation of the searches is then performed through MADANALYSIS 5 [44, 45].

Simulations have been performed in a grid of t' and S masses: $m_{t'}$ has been varied in the range 400 GeV to 1000 GeV in steps of 100 GeV, while m_S starts from a minimum value of 200 GeV and increases in steps of 100 GeV until reaching the kinematical limit $m_{t'} - m_S - m_t = 0$. A point in the small mass gap region $m_{t'} - m_S - m_t = 10$ GeV has been included as well.

The results are shown in figure 2 as upper limits on the cross section (in pb). The observed bound on the t' and S masses, represented as a solid black contour, has been obtained by comparing the upper bounds on the cross section with the cross section for pair production of t' obtained at NLO+NNLL through HATHOR [46], under the assumption of 100% BR for $t' \rightarrow St$ and for $S \rightarrow \gamma\gamma$ (figure 2 left panel) or $Z\gamma$ (figure 2 right panel) in the narrow width approximation (NWA). The range of validity of the NWA in terms of the ratio between the total width and mass of t' is discussed in appendix B.2. In the $\gamma\gamma$ channels the allowed region for $m_{t'}$ is above ~ 600 GeV almost independently of m_S . In the $Z\gamma$ channel the bounds are slightly more sensitive to the mass gap between the VLQ and the (pseudo)scalar, barring statistical fluctuations: the bound on $m_{t'}$ is however between ~ 700 GeV and ~ 800 GeV for all the allowed m_S .

The bounds obtained are typically weak compared to dedicated VLQ searches. In the next section we propose a dedicated analysis to look for the signatures we are interested in

leading to a much better sensitivity than the ones presented in figure 2.

4 Analysis

In its full generality, a top partner t' may decay into the usual three SM channels $W^+ b$, $Z t$, $h t$ or additional exotic channels. In this paper we are focusing our attention on the case of pair production $pp \rightarrow t' \bar{t}'$ and subsequent decay into the BSM channels $t' \rightarrow S t$, where S is a neutral (pseudo)scalar decaying into SM EW diboson pairs. We have chosen the decays $S \rightarrow \gamma \gamma$ and $S \rightarrow Z \gamma$ as our target signal, since they are experimentally very clean bosonic decay channels. In the case of the $Z \gamma$ channel we only consider further leptonic decays of the Z .

Our analysis strategy is based on the reconstruction of the decays product of one of the legs as depicted in figure 3 for the $S \rightarrow \gamma \gamma$ case. We assume t' decays at 100% rate as $t' \rightarrow S t$. For S , we consider all the possible bosonic decay channels necessary to ensure gauge invariance in the CHM¹,

$$S \rightarrow \{\gamma \gamma, Z \gamma, WW, ZZ\}. \quad (4.1)$$

In this section we define the objects used in the analyses (section 4.1), then describe the tools and processes for the simulation of events to model signal and background (section 4.2), and finally we present event selections to extract the signal in the two considered signal regions (SR): the $\gamma \gamma$ SR in section 4.3 and the $Z \gamma$ SR in section 4.4.

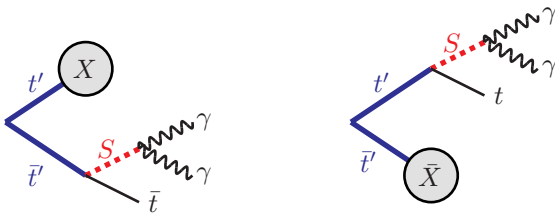


Figure 3: Pair production of t' with the decay of one branch into $t(S \rightarrow \gamma \gamma)$ and inclusive decay for the other.

4.1 Object definition

In the following details for the definition and selection of objects at reconstructed level will be presented. The default ATLAS DELPHES card [41] is used, with minor modifications. All objects with a calorimeter component that fall in the calorimeter transition region $1.37 < |\eta| < 1.53$ are excluded. Here η is the pseudorapidity which is defined as

$$\eta = -\ln \left[\tan \left(\frac{\theta}{2} \right) \right], \quad (4.2)$$

¹Note that additional decays are present for the 2HDM+VLQ case, specifically, $b\bar{b}$ and $t\bar{t}$, which are then simulated for the corresponding signal.

where θ is the angle between the object's momentum and the positive direction of the beam axis. Relative angular distances in the detector are typically expressed as ΔR ,

$$\Delta R_{12} = \sqrt{(\eta_1 - \eta_2)^2 + (\phi_1 - \phi_2)^2}, \quad (4.3)$$

where 1 and 2 are the two particles and ϕ is the azimuthal angle around the beampipe. A particle's transverse momentum p_T is the momentum component in the plane transverse to the beam axis.

Isolation and overlap removal are needed to distinguish the objects from each other in the detector simulation², which is done in the DELPHES card, unless otherwise specified. This is achieved by creating the containers for the objects in mind: jets, photons, electrons and muons. In DELPHES all objects passing their respective efficiency cut are first reconstructed as the respective object and as a jet. The object will then be put into the jet container and the container corresponding to the reconstructed object. By passing an isolation criterion the object is removed from the jet container and only kept in the container corresponding to the correct reconstruction. The criterion is met when an isolation variable I is within a certain constraint. The variable is defined by summing the p_T of all objects, not including the candidate, within a cone of ΔR around the candidate and dividing by the candidate p_T . That is,

$$I = \frac{\sum_{i \neq \text{candidate}} p_T(i)}{p_T(\text{candidate})}, \quad (4.4)$$

where the sum runs over all the objects i around the candidate within the ΔR cone.

The objects used in the analysis are defined below.

Photons, γ , are reconstructed by considering energy deposits in the electromagnetic calorimeter (ECAL) and no tracks in the inner detector. Objects successfully reconstructed as photons are required to have a $p_T > 30$ GeV and $|\eta| < 2.37$. Photons in the transition region are not taken into account. Overlap removals are done in the modified DELPHES card as described above, where the photon candidate is identified and put in the correct container by passing the photon efficiency cut corresponding to the ATLAS tight quality efficiency cuts [47]. Isolation of the photon is done after the simulation and it is considered isolated when the isolation variable $I < 0.008$, where I is defined as described above.

Leptons, ℓ , are in the following understood to mean electrons or muons only, and not τ -leptons. Electrons are reconstructed by looking at both energy deposit in the ECAL and having a track in the inner tracking system. For the following, simulation in DELPHES reconstruction of the electron is done by combining the reconstruction efficiency of the two subsystems and parametrise it as a function of energy and pseudorapidity. Muons pass the calorimeters and are reconstructed by combining the information from the inner tracker and the muon spectrometer. In DELPHES, the user specifies the efficiency of the muons such that a muon is only reconstructed with a certain probability [41]. Leptons are required to pass an isolation criterion for which $I < 0.12$ within the cone $\Delta R < 0.2$ for electrons and

²In detectors at colliders, the same energy deposits can be associated with different objects, e.g., an electron can also be identified as a jet. In order to make sure each energy deposit is counted only once, every object has to be energetically isolated and the objects are not allowed to overlap in the detector.

$\Delta R < 0.3$ for muons. Furthermore, leptons are required to have $p_T > 25$ GeV and be in the region of $|\eta| < 2.47$, excluding the transition region in the case of electrons. Further overlap removals of leptons are done in DELPHES where the lepton candidate is identified and put into the correct container by passing the given lepton efficiency. For electrons, the efficiencies correspond to the ATLAS tight quality efficiency cut [48]. For muons, the default DELPHES values are used.

Z bosons, Z are identified as two same-flavour opposite-sign leptons whose invariant mass fall within the window $|M_{\ell+\ell^-} - m_Z| < 10$ GeV where $M_{\ell+\ell^-}$ is the invariant mass of the reconstructed leptons.

Jets, j , are reconstructed by using the FASTJET [49] package together with DELPHES. Here the anti- k_t algorithm [50] with a R parameter of $R = 0.4$ is in use for jet reconstruction. Jets are required to pass $p_T > 25$ GeV and $|\eta| < 2.47$, excluding the transition region.

B-jets, j_b , are jets which originate from the hadronisation of a b -quark. In DELPHES this means a jet which contains a truth b -quark. The efficiency and misidentification rate is parametrised in DELPHES based on estimates from ATLAS [41, 51].

Missing transverse energy, E_T^{miss} , is computed in DELPHES by taking the negative scalar sum of the transverse component of the momenta of all calorimeter towers (i.e., energy deposits in the calorimeter), $\vec{E}_T^{\text{miss}} = -\sum_i \vec{p}_T(i)$ [41].

The scalar transverse energy, H_T , is computed by taking the scalar sum of the p_T of all reconstructed basic objects used in the analysis, in this case: jets, muons, electrons and photons. All these objects which enter the H_T definition are required to pass the stated analysis p_T and η cuts.

4.2 Simulations

All simulations in this study have been performed using the following framework: MADGRAPH 5_AMC@NLO [38] was used to generate events at leading order accuracy. PYTHIA 8.2 [40] and DELPHES 3 [41] have been used for showering and fast detector simulation, respectively. For the signal simulations, the parton distribution function (PDF) NNPDF 3.1 at NLO set [42] set has been chosen, obtained through the LHPDF 6 library [43] using PDF ID 303400. For the background simulations instead the MADGRAPH default NNPDF 2.3 LO with PDF ID 230000 has been used.

The numerical values of the pair production cross-sections, which only depend on m_ν , are shown in figure 4. They were computed through HATHOR [46], with NNLO MSTW2008 [52] PDFs.

The background of the $\gamma\gamma$ SR is dominated by $pp \rightarrow \gamma\gamma + \text{jets}$ mediated by QCD interactions. Events from this process are generated with up to three jets, including jets initiated by b -quarks, in the matrix element. The final jets after showering and jet clustering are matched to the original partons with the MLM method [53] as implemented in PYTHIA. In the simulation of the initial state b -quarks are explicitly considered as part of the incoming protons. This accounts for processes with an odd number of b -jets in the final state, such as those initiated by $gb \rightarrow \gamma\gamma + u\bar{b}$. To ensure enough statistics in the high mass tail the events are generated in slices of the diphoton invariant mass $M_{\gamma\gamma}^{\text{bkg}}$ with ~ 1 M events per slice, where $M_{\gamma\gamma}^{\text{bkg}}$ refers to the invariant mass of the generated (not reconstructed) photons.

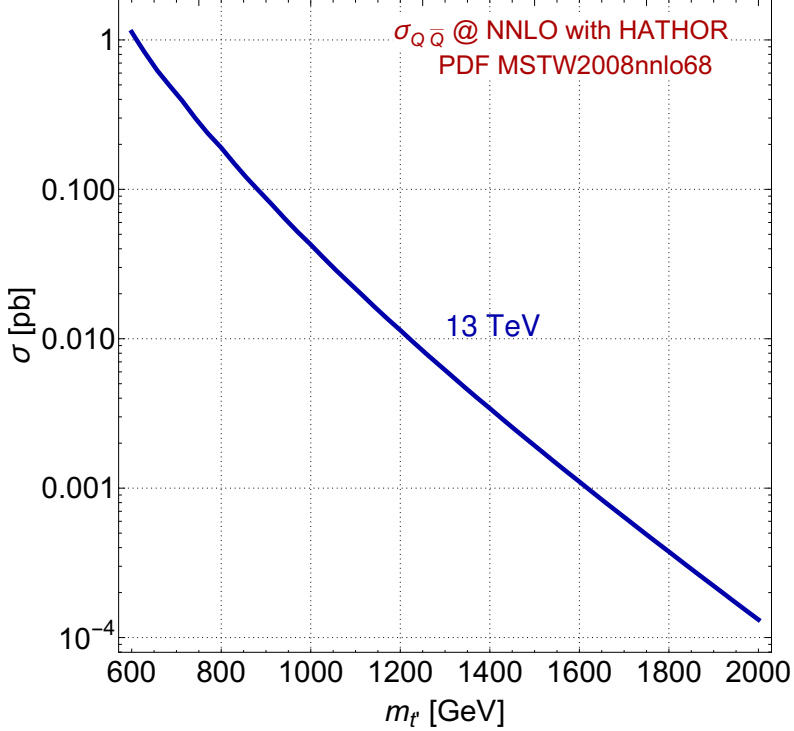


Figure 4: Pair production cross section of t' at NLO+NNLL computed through HATHOR [46], with NNLO MSTW2008 [52] PDFs.

Table 1 lists the slices along with the fiducial cross section for each slice. The invariant mass of the two photons for all slices is shown in figure 5. If there are more than two photons in the event, the pair with invariant mass closer to 160 GeV is shown in this figure. The total fiducial cross section in the $M_{\gamma\gamma}^{\text{bkg}} > 50$ GeV region is calculated by generating 25K events in the allowed range using the same setup as in the full event generation, resulting in 74.0 pb, in good agreement with the sum of the fiducial cross sections for the individual slices.

The dominant background in the $S \rightarrow Z\gamma$ final state is $pp \rightarrow Z\gamma + \text{jets}$, with $Z \rightarrow \ell^+\ell^-$. Events from this process are generated using the same setup as for the $\gamma\gamma + \text{jets}$ background, with up to two hard jets in the matrix elements. For the same reason as for $\gamma\gamma + \text{jets}$ the event generation for the $Z\gamma + \text{jets}$ background is performed in slices of the invariant mass of the generator-level Z and γ , $M_{Z\gamma}^{\text{bkg}}$, with $\sim 2\text{M}$ events each, listed in table 1 together with their fiducial cross section. The latter at $M_{Z\gamma}^{\text{bkg}} > 50$ GeV is estimated to be 4.451 pb by generating 25K events in the allowed kinematic range, which, again, is in good agreement with the sum of the fiducial cross sections of the slices. SM top-quark pair production associated to a photon and to a Z and a photon can also give relevant contributions to the background. We generated 150K events of the process $t\bar{t} + Z\gamma$ and let the top decay inclusively and the Z leptonically via MADSPIN. For $t\bar{t} + \gamma$ we generated 300K events and required the top quarks to decay leptonically to either electrons or muons. We use the LO cross sections 0.315 fb for decayed $t\bar{t} + Z + \gamma$ and 94 fb for decayed $t\bar{t} + \gamma$ events. The

| Background process | $\sigma_{\text{fid.}}(\gamma\gamma + \text{jets})$ [pb] | $\sigma_{\text{fid.}}(Z\gamma + \text{jets})$ [pb] |
|--------------------|---|--|
| 50 – 150 GeV | 69.0 ± 0.2 | 3.223 ± 0.003 |
| 150 – 250 GeV | 3.577 ± 0.006 | 1.010 ± 0.001 |
| 250 – 500 GeV | $(91.3 \pm 0.2) \times 10^{-2}$ | $(22.56 \pm 0.02) \times 10^{-2}$ |
| 500 – 1000 GeV | $(99.2 \pm 0.2) \times 10^{-3}$ | $(25.43 \pm 0.03) \times 10^{-3}$ |
| 1000 – 1500 GeV | $(63.6 \pm 0.2) \times 10^{-4}$ | $(1.764 \pm 0.002) \times 10^{-3}$ |
| Sum | 73.6 ± 0.1 | 4.486 ± 0.003 |
| Estimated total | 74.0 ± 0.6 | 4.45 ± 0.03 |

Table 1: Fiducial cross section for each mass slice of the two major background processes. For the $\gamma\gamma + \text{jets}$ background the slices refer to $M_{\gamma\gamma}^{\text{bkg}}$ while for the $Z\gamma + \text{jets}$ background the slices refer to $M_{Z\gamma}^{\text{bkg}}$ at the generator level. The sums of the fiducial cross sections over all slices for each process are also listed together with their estimated value.

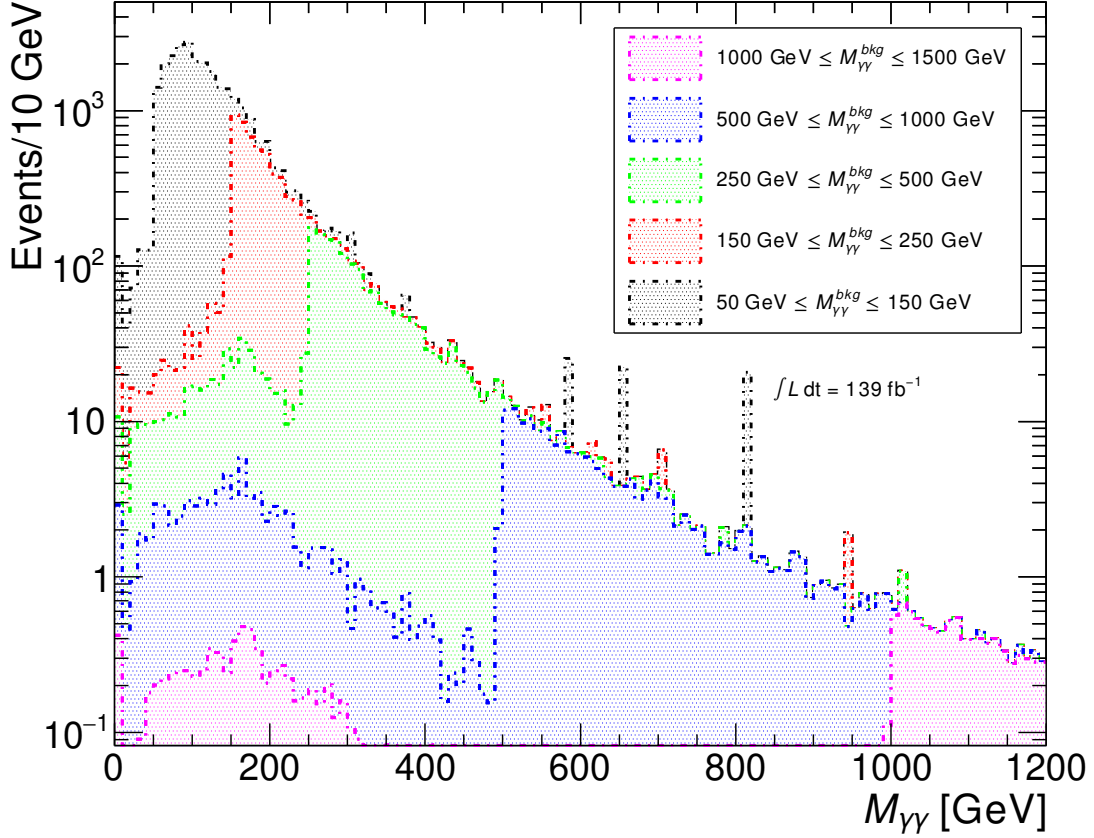


Figure 5: Invariant mass $M_{\gamma\gamma}$ of the photon pair at reconstructed level for each $M_{\gamma\gamma}^{\text{bkg}}$ slice in the $\gamma\gamma + \text{jets}$ background. At least two photons and one b -jet, as defined in section 4.1, are required.

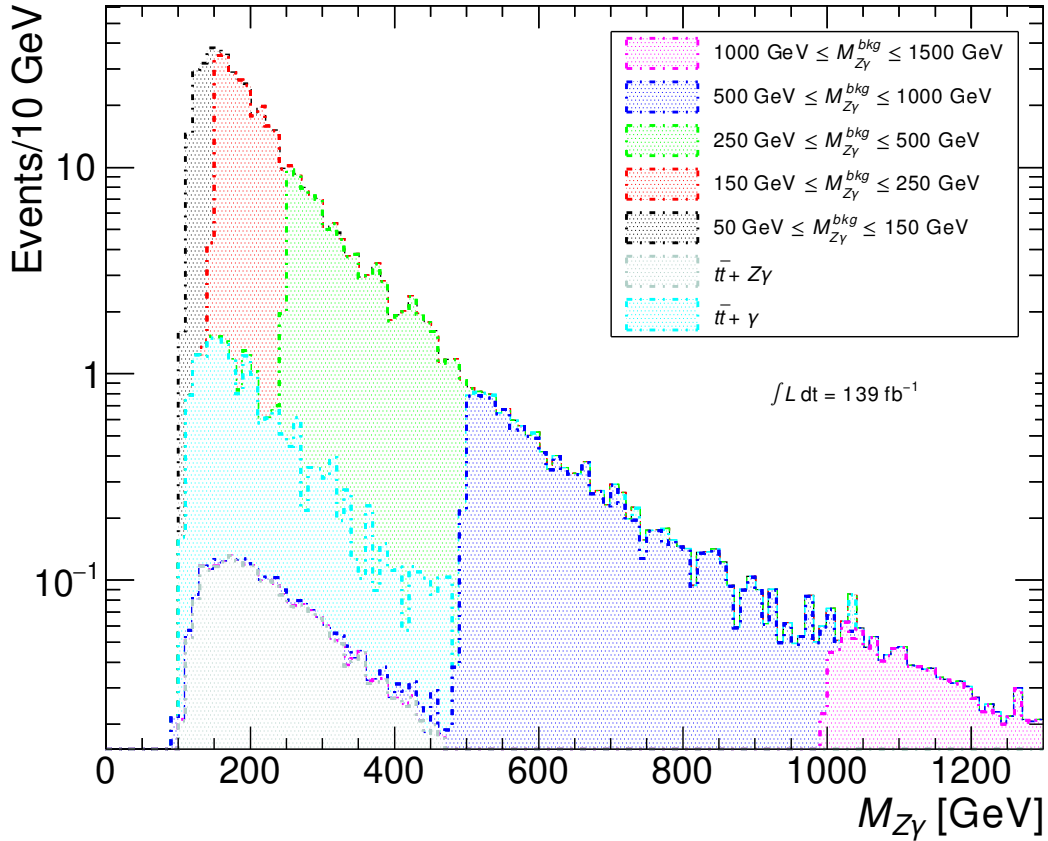


Figure 6: Invariant mass $M_{Z\gamma}$ of the reconstructed Z boson and the photon for each mass slice in the $Z\gamma + \text{jets}$ background, as well as for the $t\bar{t} + \gamma$ and $t\bar{t} + Z + \gamma$ backgrounds. At least one Z boson, one photon and one b -jet, as defined in section 4.1, are required.

invariant mass of the $Z\gamma$ system, for each of the mass slices of $Z\gamma + \text{jets}$, together with $t\bar{t} + \gamma$ and $t\bar{t} + Z + \gamma$, is shown in figure 6. In that figure, at least one Z boson, one photon and one b -jet, according to the definitions in section 4.1, are required. If there are more than one Z and/or γ candidate we choose the system with invariant mass closer to 160 GeV to present in this specific plot.

In both final states, non-prompt backgrounds are also possible. These are expected to be reduced significantly since we use tight identification requirements for leptons and photons. Furthermore, in analyses with similar final states, the backgrounds with one or more jets mis-identified as photons was found to be significantly smaller than those with prompt photons [54]. Thus, we do not consider non-prompt background sources in either of the final states.

For the signal simulation and definition, we generated the process $pp \rightarrow t't'$ with $t' \rightarrow St$ and S decaying into EW bosons, eq. (4.1). We define our signal samples as any possible decay combination, $(S \rightarrow X)(S \rightarrow Y)$ where $X, Y \in \{\gamma\gamma, Z\gamma, WW, ZZ\}$. Both the Z and W decay inclusively in our signal definition.

The UFO model for signal simulations is the same one used for recasting LHC bounds, corresponding to the simplified Lagrangian of eq. (2.1). Decays of interest are thus turned on or off by setting the corresponding couplings. In the following analysis, couplings are set such that the widths for the top partner t' and scalar S are 0.1% of their mass, to allow the use of the NWA (see also appendix B.2). For the simulations, we use $\kappa_S^R = 0$, keeping only κ_S^L coupling. Similarly we turn off the scalar S couplings, $\kappa_W = \kappa_B = \lambda_W = \lambda_Z = 0$, when we assume a pseudoscalar nature of the S state. However, there is no difference in our predictions with respect to a scalar S , but a different top coupling can lead to differences, as discussed in appendix B.1. In view of this indistinguishability, in the 2HDM+VLQ case, we will assume the S state to represent degenerate CP-even and CP-odd neutral Higgs states entering the t' decay.

4.3 $S \rightarrow \gamma\gamma$ signal region

In this section, the diphoton final state is presented. From an experimental point of view, the diphoton final state gives a very clean signature in the detector, which makes it attractive to study.

We considered t' masses $m_{t'} = 600$ to 1800 GeV in steps of 200 GeV, every kinematically allowed S mass is investigated, via the discrete values of $m_S = 100$ GeV, 200 GeV, 400 GeV, and then in steps of 200 GeV up to the highest kinematically available mass, $m_S = m_{t'} - 200$ GeV. The wide selection of S and t' masses enables the possibility to study both threshold effects and highly boosted decay products.

To select the signal we demand the presence of 2 photons and 1 b -jet defined according to section 4.1. If more than one pair of photons is present we choose the pair whose invariant mass is closer to m_S and define these photons as “best” photon candidates, γ_1, γ_2 . Unless otherwise specified, a pair of photons is assumed to be the “best” pair. The invariant mass of the system with the two “best” photon candidates is required to be within 20 GeV from the nominal S mass, $|M_{\gamma\gamma} - m_S| < 20$ GeV.

In order to further enhance the signal discrimination with respect to the background for low m_S values we use the fact that the S is produced in a *boosted* regime. The top partners t' and \bar{t}' will be produced nearly at rest and the pair will be back-to-back. The large difference in mass between t' and S will make S boosted and thus also the photon pair from S will be collimated. In figure 7 we show the $\Delta R_{\gamma\gamma}$ distributions for different m_S and for $m_{t'} = 800$ GeV fixed. We take advantage of this characteristic signal profile and require $\Delta R_{\gamma\gamma} < 2.3$ from $m_S = 100$ GeV to $m_S = 200$ GeV.

The selection cuts are summarised in table 2. Note that, due to limitations in statistics, the cuts are sub-optimal. The discrimination between signal and background could be improved significantly by tightening the cuts in a real experimental analysis.

In table 3 we show the efficiencies (number of events left after the cut divided by the number before the cut) of the selection cuts numbered in table 2 for different m_S values. In the upper part of the table, the signal process is defined with both S decaying into diphotons, i.e., $t\bar{t}S(\rightarrow \gamma\gamma)S(\rightarrow \gamma\gamma)$ in the final state. This is the process we use to optimise the selection cuts. We display only the $m_{t'} = 1$ TeV case in the table. In the lower part of the table, the efficiencies for the background sample are displayed, which do

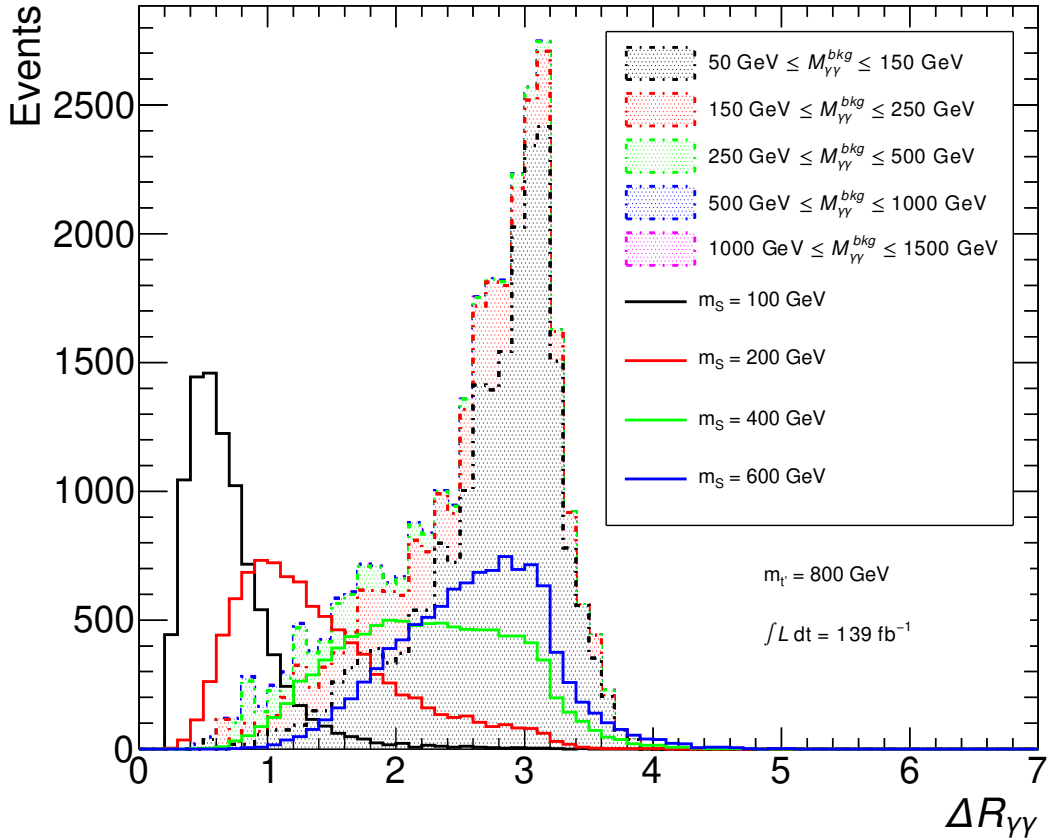


Figure 7: Distributions of $\Delta R_{\gamma\gamma}$ of the two photons with invariant mass closest to m_S , at the reconstructed level, with $m_{t'} = 800$ GeV and various m_S values. In the plot, cuts 1 and 2, as defined in table 2, have been applied.

| Cut no. | Description |
|---------|---|
| 1 | $N_\gamma \geq 2$ |
| 2 | $N_{\text{b-jets}} \geq 1$ |
| 3 | $ M_{\gamma\gamma} - m_S < 20$ GeV |
| 4 | $\Delta R_{\gamma\gamma} < 2.3$ ($m_S \leq 200$ GeV) |

Table 2: Selection cuts applied to the $S \rightarrow \gamma\gamma$ signal region. The cuts are described in detail in the text. Refer to section 4.1 for the definition of the objects.

not depend on $m_{t'}$. It can be noticed that the last two cuts are the most efficient ones in removing the background and keeping signal events.

The final efficiencies for the signal decay channel $S(\rightarrow \gamma\gamma)S(\rightarrow \gamma\gamma)$ are discussed in section 4.5. The efficiencies for the other signal decay channels with at least one branch decaying into $\gamma\gamma$ are presented in appendix C.

| m_S | 100 GeV | 200 GeV | 400 GeV | 600 GeV | 800 GeV |
|---------|--|----------------------|----------------------|----------------------|----------------------|
| Cut no. | Signal $t\bar{t}(S \rightarrow \gamma\gamma)(S \rightarrow \gamma\gamma)$ efficiency (%) | | | | |
| 1 | 98.1 | 98.8 | 99.1 | 99.0 | 98.8 |
| 2 | 48.8 | 47.9 | 51.0 | 54.8 | 60.4 |
| 3 | 35.9 | 35.9 | 39.4 | 42.9 | 46.4 |
| 4 | 35.8 | 34.0 | 39.4 | 42.9 | 46.4 |
| Cut no. | Background efficiency (%) | | | | |
| 1 | 15.4 | 15.4 | 15.4 | 15.4 | 15.4 |
| 2 | 2.8×10^{-1} | 2.8×10^{-1} | 2.8×10^{-1} | 2.8×10^{-1} | 2.8×10^{-1} |
| 3 | 5.7×10^{-2} | 1.2×10^{-2} | 1.1×10^{-3} | 2.5×10^{-4} | 7.1×10^{-5} |
| 4 | 2.0×10^{-2} | 1.9×10^{-3} | 1.1×10^{-3} | 2.5×10^{-4} | 7.1×10^{-5} |

Table 3: Signal and background efficiencies in percent following the cuts listed in table 2, for the $\gamma\gamma$ SR and $m_{\mu'} = 1000$ GeV.

4.4 $S \rightarrow Z\gamma$ signal region

In the $S \rightarrow Z\gamma$ final state we require at least one Z boson candidate reconstructed according to the definitions in section 4.1. In addition to the Z candidate we require the presence of at least one isolated photon. The system of one isolated photon and one Z candidate whose invariant mass is closest to the nominal S mass is called the “best S candidate”. To efficiently distinguish the signal from the background we exploit the high multiplicity of objects and high total energy of a typical signal event. We require $H_T + E_T^{\text{miss}} > 0.3m_{\mu'}$, where H_T is the scalar sum of the p_T of all reconstructed basic objects and E_T^{miss} is the missing transverse energy of the event as described in section 4.1. We finally require the invariant mass of the S candidate to be within 15 GeV of the nominal S mass, i.e., $|M_{Z\gamma} - m_S| < 15\text{GeV}$. A summary of these selection cuts is presented in table 4, with some information on the object definitions for convenience.

The distributions of $M_{Z\gamma}$ before cut 5 and $H_T + E_T^{\text{miss}}$ before cut 4 and 5 are shown in figure 8, for the masses $m_S = 160$ GeV and $m_{\mu'} = 1400$ GeV. There is a great discriminating power in the $H_T + E_T^{\text{miss}}$ observable due to the large multiplicity and energy of a typical signal event. We note that the used cut is not optimised to suppress the background due to lack of MC statistics. A realistic experimental analysis could harden this cut to further reduce the background and use data-driven methods to estimate it without relying too much on MC estimates.

For illustrative purposes, in table 5, we show the efficiencies of the selection cuts numbered in table 4 for different m_S values. We display only the case $m_{\mu'} = 1400$ GeV in the table. In the upper subtable, the signal process is defined with both S decaying into $Z\gamma$, $S(\rightarrow Z\gamma)S(\rightarrow Z\gamma)$ in the final state. This is the process we use to optimise the selection cuts. In the lower subtable, the efficiencies for the background sample are displayed. Differently from the $\gamma\gamma$ SR, here the cuts, and thus the efficiencies for the background, depend on $m_{\mu'}$. We can notice however that only the last cut depends on the value of m_S .

In figure 9 (right) we show the final efficiency in the $Z\gamma$ SR (after cut 5) for the signal

| Cut no. | Description |
|---------|--|
| 1 | $N_Z \geq 1$ |
| 2 | $N_\gamma \geq 1$ |
| 3 | $N_{\text{b-jets}} \geq 1$ |
| 4 | $H_T + E_T^{\text{miss}} > 0.3m_{t'}$ |
| 5 | $ M_{Z\gamma} - m_S < 15 \text{ GeV}$ |

Table 4: Selection cuts applied to the $Z\gamma$ signal region. Details on the cuts are given in the text. Refer to section 4.1 for the definition of the objects.

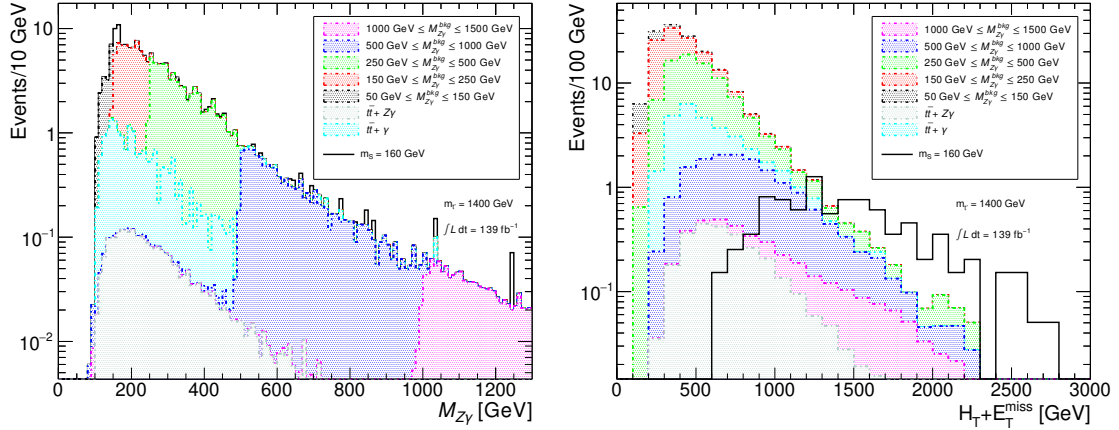


Figure 8: Distributions of $M_{Z\gamma}$ and $H_T + E_T^{\text{miss}}$ for $m_S = 160 \text{ GeV}$ and $m_{t'} = 1400 \text{ GeV}$.

| m_S | 130 GeV | 160 GeV | 400 GeV | 800 GeV |
|---------|--|-----------------------|-----------------------|-----------------------|
| Cut no. | Signal ($S \rightarrow Z\gamma$)($S \rightarrow Z\gamma$) efficiency (%) | | | |
| 1 | 4.11 | 4.81 | 5.80 | 5.68 |
| 2 | 2.74 | 3.97 | 5.39 | 5.13 |
| 3 | 1.51 | 2.31 | 3.27 | 3.61 |
| 4 | 1.51 | 2.31 | 3.27 | 3.61 |
| 5 | 1.19 | 1.77 | 2.43 | 2.36 |
| Cut no. | Background efficiency (%) | | | |
| 1 | 21.7 | 21.7 | 21.7 | 21.7 |
| 2 | 4.13 | 4.14 | 4.14 | 4.14 |
| 3 | 0.0731 | 0.0731 | 0.0731 | 0.0731 |
| 4 | 0.0461 | 0.0463 | 0.0463 | 0.0463 |
| 5 | 5.22×10^{-3} | 8.09×10^{-3} | 9.39×10^{-4} | 6.81×10^{-5} |

Table 5: Signal and background efficiencies in percent following the cuts listed in table 4, for the $Z\gamma$ SR and $m_{t'} = 1000 \text{ GeV}$.

decay channel $S(\rightarrow Z\gamma)S(\rightarrow Z\gamma)$. The efficiencies for the other signal decay channels with at least one branch decaying into $Z\gamma$ are presented in appendix C.

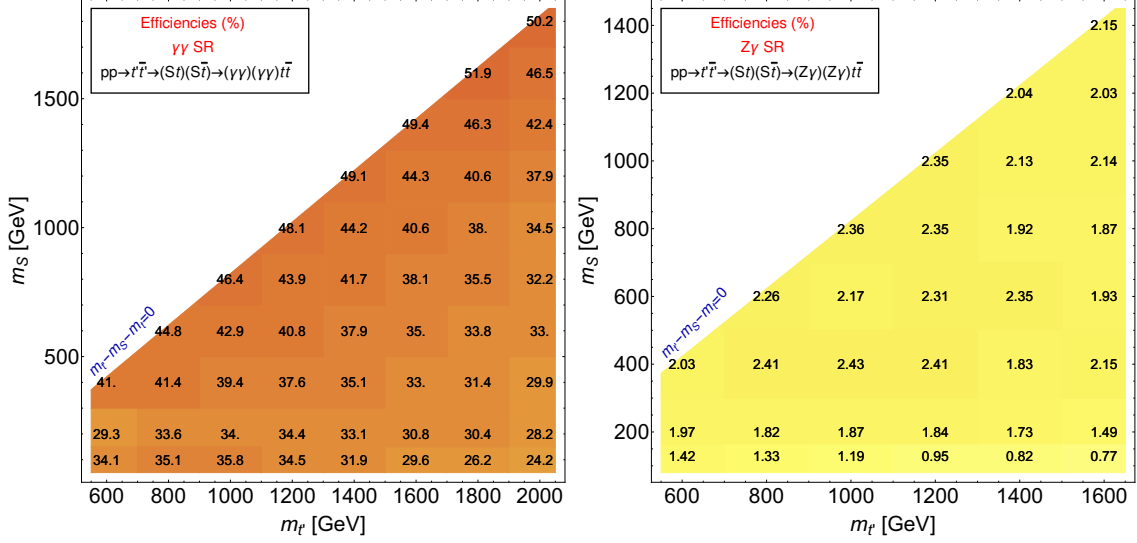


Figure 9: Left: Efficiencies for the $\gamma\gamma$ SR for the signal decay channel $S(\rightarrow\gamma\gamma)S(\rightarrow\gamma\gamma)$. Right: Efficiencies for the $Z\gamma$ SR for the signal decay channel $S(\rightarrow Z\gamma)S(\rightarrow Z\gamma)$.

4.5 Efficiencies

The signal efficiencies for the two different signal regions are the last piece of information necessary for reconstructing the number of signal events. In figure 9 we provide, as illustrative examples, the efficiencies for the $(\gamma\gamma)(\gamma\gamma)$ channel in the $\gamma\gamma$ SR and for the $(Z\gamma)(Z\gamma)$ channel in the $Z\gamma$ SR, for which the selections have been optimised. Further efficiency plots for different channels are provided in appendix C. All efficiencies have been computed considering signal samples of 10^4 MC events, corresponding to a statistical uncertainty of the order of 10% which can affect the evaluation of efficiencies especially when they are small. The whole set of efficiencies, combined with the BRs chosen in section 4, allows one to compute the expected total number of events via eq. (5.2) in the following section, where the results of the study are discussed.

In the next section we will show how to estimate the number of events for both signal and backgrounds for different model assumptions and devise a simple statistical framework for model interpretation.

5 Results

In this section we discuss the discovery potential of LHC for the models introduced previously. Essentially, we propose a counting experiment comparing the number of expected background events with the number of signal events.

The expected number of background events in one of the signal regions $\text{SR} \in \{\gamma\gamma, Z\gamma\}$, B_{SR} , is given by

$$B_{\text{SR}}(m_S, m_{t'}) = L \sigma_{B_{\text{SR}}} \epsilon_{B_{\text{SR}}}(m_S, m_{t'}) \quad (5.1)$$

with L the integrated luminosity, and $\sigma_{B\gamma\gamma} = 74.0$ pb and $\sigma_{BZ\gamma} = 4.58$ pb our best estimate of the total background cross section for the $\gamma\gamma$ and $Z\gamma$ signal regions, respectively, and $\epsilon_{B_{\text{SR}}}$ the efficiency after all cuts in the corresponding SR.

The number of background events can be extracted for arbitrary values of m_S and $m_{t'}$ by interpolating the data presented in tables 6–7.

| m_S [GeV] | $\sigma_{B\gamma\gamma}\epsilon_{B_{\text{SR}}}(m_S)$ [pb] |
|-------------|--|
| 100 | 0.0146 |
| 200 | 0.00144 |
| 400 | 8.41×10^{-4} |
| 600 | 1.82×10^{-4} |
| 800 | 5.23×10^{-5} |
| 1000 | 2.14×10^{-5} |
| 1200 | 7.64×10^{-6} |
| 1400 | 3.10×10^{-6} |

Table 6: The background cross section times efficiency $\sigma_{B\gamma\gamma}\epsilon_{B\gamma\gamma}(m_S)$ (in pb) relevant for the $\gamma\gamma$ signal region. For this signal region the efficiency is independent of $m_{t'}$.

| m_S [GeV] | $m_{t'}$ [GeV] | | | | | |
|-------------|-----------------------|-----------------------|-----------------------|-----------------------|-----------------------|-----------------------|
| | 600 | 800 | 1000 | 1200 | 1400 | 1600 |
| 130 | 5.87×10^{-4} | 3.94×10^{-4} | 2.39×10^{-4} | 1.39×10^{-4} | 7.32×10^{-5} | 5.15×10^{-5} |
| 160 | 7.61×10^{-4} | 5.90×10^{-4} | 3.70×10^{-4} | 2.34×10^{-4} | 1.54×10^{-4} | 9.65×10^{-5} |
| 200 | 4.79×10^{-4} | 4.37×10^{-4} | 3.47×10^{-4} | 2.47×10^{-4} | 1.47×10^{-4} | 9.48×10^{-5} |
| 400 | 4.55×10^{-5} | 4.42×10^{-5} | 4.30×10^{-5} | 4.10×10^{-5} | 3.75×10^{-5} | 3.24×10^{-5} |
| 600 | | 9.98×10^{-6} | 9.88×10^{-6} | 9.72×10^{-6} | 9.39×10^{-6} | 8.96×10^{-6} |
| 800 | | | 3.12×10^{-6} | 3.12×10^{-6} | 3.05×10^{-6} | 3.02×10^{-6} |
| 1000 | | | | 1.16×10^{-6} | 1.11×10^{-6} | 1.11×10^{-6} |
| 1200 | | | | | 5.01×10^{-7} | 4.94×10^{-7} |
| 1400 | | | | | | 2.17×10^{-7} |

Table 7: The background cross section times efficiency $\sigma_{BZ\gamma}\epsilon_{BZ\gamma}(m_S, m_{t'})$ (in pb) relevant for the $Z\gamma$ signal region.

It should be noted that we only present the estimates for the irreducible background. This turns out to be negligible in the high mass region and its values are presented only to show this fact and for completeness. In this region, fake rates are likely to become relevant but they can be reliably estimated only by the experimental collaborations.

The number of expected signal events for each SR is given by

$$S_{\text{SR}} = L \sigma(m_{t'}) \left(\sum_{X,Y} \epsilon_{\text{SR}}^{Y,X} \text{BR}_{S \rightarrow X} \text{BR}_{S \rightarrow Y} \right), \quad (5.2)$$

where $\epsilon_{\text{SR}}^{Y,X}$ is the final efficiency in appropriate signal region SR for the signal sample with decay $(S \rightarrow X)(S \rightarrow Y)$ with $X, Y \in \{\gamma\gamma, Z\gamma, WW, ZZ\}$. (In these expressions we assume the validity of the NWA and assume 100% BR $t' \rightarrow St$ and $\bar{t}' \rightarrow S\bar{t}$.)

In appendix C we tabulate the above efficiencies, allowing one to estimate the signal in any of the theoretical models discussed here by simply computing the corresponding BR. The discovery potential for a more generic model can be also estimated using the numbers provided as long as the efficiency times BR of any extra decay channel is known to be small.

Having computed the number of signal (S) and background (B) events, we estimate the significance by employing the formula [55–57]

$$z = \sqrt{2} \left\{ (S + B) \ln \left[\frac{(S + B)(B + \sigma_b^2)}{B^2 + (S + B)\sigma_b^2} \right] - \frac{B^2}{\sigma_b^2} \ln \left[1 + \frac{\sigma_b^2 S}{B(B + \sigma_b^2)} \right] \right\}^{1/2}, \quad (5.3)$$

that is obtained by using the ‘‘Asimov’’ data-set into the profile likelihood ratio. The explicit expression above, containing the uncertainty σ_b on the background, is found in ref. [58].

We consider an overall $\sigma_b = 10\%B$ systematic uncertainty on B . This number is most likely a conservative estimate and it is estimated by comparing the systematic uncertainties of ATLAS and CMS analyses with similar final states, especially high-mass $Z\gamma$ searches [59, 60] and high mass $\gamma\gamma$ searches [61–63].

5.1 Model interpretation

Recall that the main focus is the study of models where the top partner has 100% BSM BR $t' \rightarrow St$ and S decays into EW gauge bosons. Even within this limited framework, we still need to discuss the relative strengths of the various S decay channels, controlled by the couplings in eq. (2.1).

We start by considering the optimal reaches for the two SR considered in this analysis, corresponding to scenarios where S decays fully either into $\gamma\gamma$ or $Z\gamma$. Such scenarios are likely non-physical, but they allow to determine the maximum potential of the selections. The LHC reaches for this simplified scenario are presented in figure 10 for two different LHC luminosities, corresponding to the final luminosity at the end of Run II and the nominal final luminosity of Run III.

We further consider two benchmark scenarios, motivated by partial compositeness, where only the pseudoscalar couplings $\tilde{\kappa}_B$ and $\tilde{\kappa}_W$ to EW bosons field strengths are active. (The scalar case gives almost identical results.) We pick two representative values chosen for their simplicity and also because they are representative of the two main discovery channels we chose.

In the first scenario, we set $\tilde{\kappa}_B + \tilde{\kappa}_W = 0$, thus suppressing the $S \rightarrow \gamma\gamma$ decay, leading to a 100% BR $_{S \rightarrow Z\gamma}$ below the WW threshold and still an acceptably large value above it. The dependence of the BRs on the S mass are shown, for the pseudoscalar case, in figure 11 (left). The LHC reaches for this scenario are presented in figure 11 (right) for two different LHC luminosities, corresponding to the final luminosity at the end of Run II and the nominal final luminosity of Run III. Here, we consider only the $Z\gamma$ SR because of the negligible sensitivity of the $\gamma\gamma$ SR.

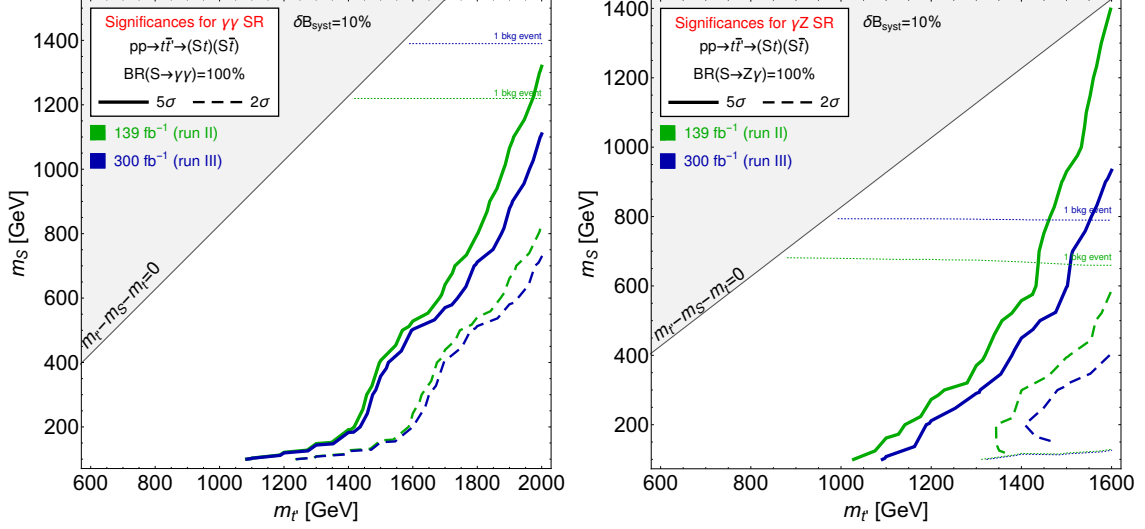


Figure 10: LHC optimal reach for different LHC luminosities for the $\gamma\gamma$ SR (left) and $Z\gamma$ SR (right). The solid lines correspond to the 5 σ discovery reach, while the dashed lines correspond to the 2 σ exclusion reach. The dotted lines identify the region with 1 irreducible background event, where the contribution of fake rates can become relevant.

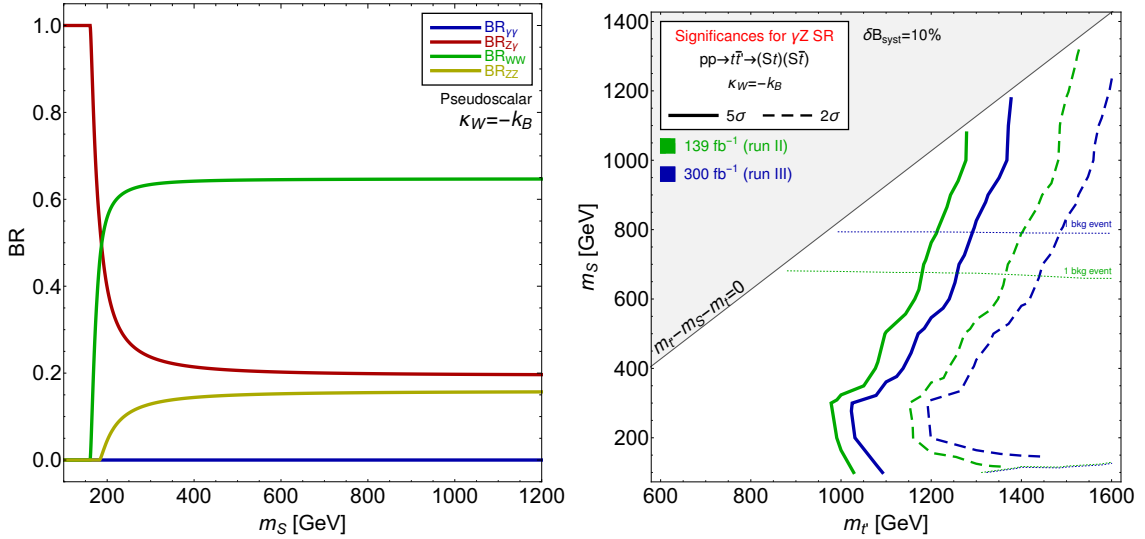


Figure 11: Left panel: BRs of S resonance into EW bosons for the pseudoscalar case ($\kappa_B = \kappa_W = 0$) in the photophobic S case ($\tilde{\kappa}_B = -\tilde{\kappa}_W$). Right panel: LHC reach for different LHC luminosities; the meaning of contours is the same as in figure 10.

In the second scenario, we choose $\kappa_W = 0$, leading to a large $BR_{S \rightarrow \gamma\gamma}$ throughout the mass range for the S and a suppression of the decay into W bosons. For the W -phobic case we estimate the LHC reaches using the more sensitive diphoton analysis. The BRs and significances are shown in the left and right panels of figure 12 respectively.

The interpretation for the composite Higgs model described in section 2.3 is straight-

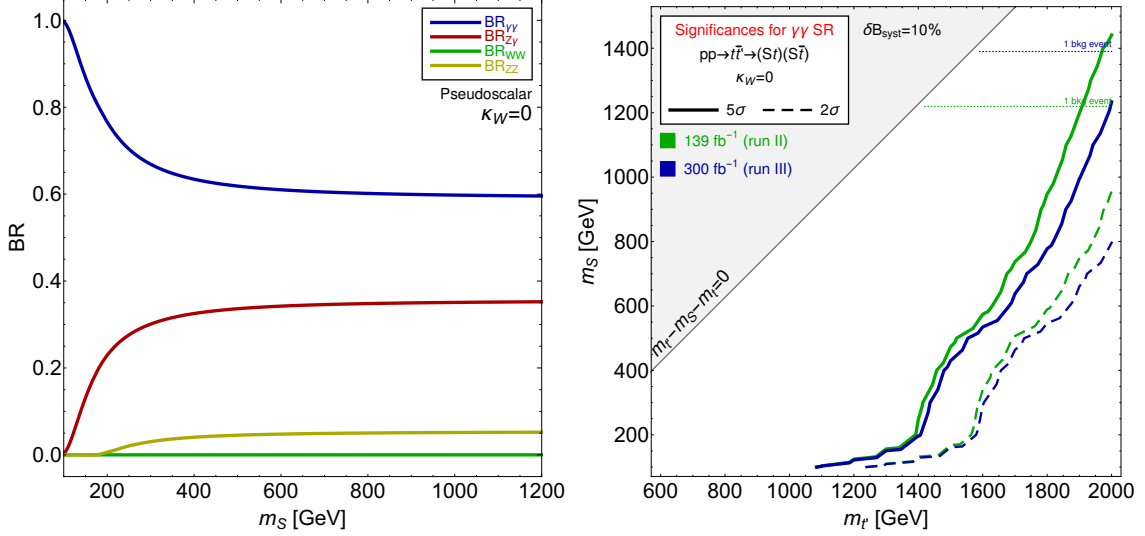


Figure 12: Left panel: BRs of S resonance into EW bosons for the pseudoscalar case ($\kappa_B = \kappa_W = 0$) in the W -phobic case ($\tilde{\kappa}_W = 0$). Right panel: LHC reach for different LHC luminosities; the meaning of contours is the same as in figure 10.

forward. The S is photophobic and we can read the bounds directly from the left panel of figure 10. It is encouraging to see that even for not optimised cuts this channel could be competitive with the search for the $+5/3$ charged partner [11]. Some more details for this model are given in appendix A.

For the 2HDM+VLQ the interpretation is somewhat more complicated because of the more numerous parameters, richer particle spectrum and, hence, t' and S decay patterns. In fact, here, the $t' \rightarrow St$ decays (for $S = H, A$) have a 50% BR each while the $H/A \rightarrow \gamma\gamma$ and $Z\gamma$ decay rates can be sizeably enhanced by t - t' mixing effects and/or t' contributions in the fermionic loops. (More detail is presented in appendix A.) Figure 13 (left) presents the decay rates for the $\gamma\gamma$ signal³ mapped over the $(m_{t'}, m_S)$ plane, wherein S represents a superposition of degenerate H and A states (i.e., $m_H = m_A = m_S$), by fixing the remaining parameters to the representative values listed in the caption (notice the scan in s_L). Such a decay rate in the 2HDM+VLQ can reach the 5% level, particularly in the $m_S < 2m_t$ region, i.e., below the opening of the $H/A \rightarrow t\bar{t}$ decays, after which it settles around 1% (all this quite independently of $m_{t'}$).

It is also interesting to compare the rates of $\gamma\gamma$ and $Z\gamma$ against those of other Higgs decay channels in the 2HDM+VLQ. This is done in figure 13 (right) (wherein $m_{t'} = 1$ TeV and $m_H = m_A (= m_S) = 350$ GeV) for the case of H, A decays, when the BRs of the aforementioned final states are maximised, owing to the absence of $H, A \rightarrow W^+W^-$ and ZZ decays, because of the alignment limit $\sin(\beta - \alpha) = 1$ for the H and the CP-nature of the A . Even in this case, though, and despite the growth of $\text{BR}(H, A \rightarrow \gamma\gamma)$ and $\text{BR}(H, A \rightarrow Z\gamma)$ with s_L (recall that the limit $s_L \rightarrow 0$ corresponds to the ordinary 2HDM), it is clear that the signatures searched for here are subleading with respect to $b\bar{b}$ (and, starting from $m_S \approx 2m_t$,

³In this scenario, in fact, the $Z\gamma$ case affords one with no sensitivity for our chosen values of luminosity.

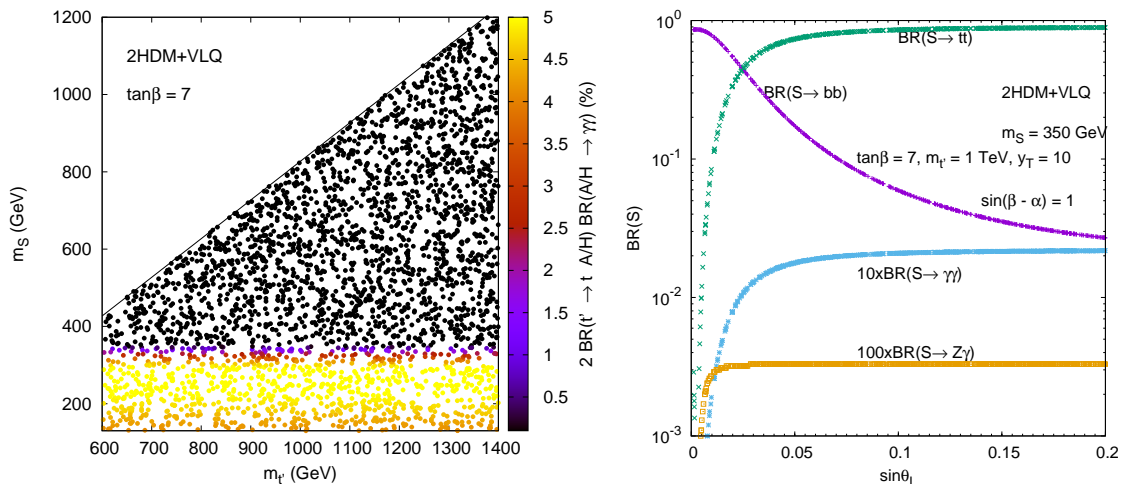


Figure 13: Left: $2 \text{BR}(t' \rightarrow tA/H) \times \text{BR}(A/H \rightarrow \gamma\gamma)$ in the 2HDM+VLQ over the plane $(m_{t'}, m_S)$, where $m_S = m_H = m_A$, for the following input parameters: $\sin(\beta - \alpha) = 1$, $m_h = 125.09 \text{ GeV}$, $m_{H^\pm} = 600 \text{ GeV}$, $\tan\beta = 7$, $m_{12}^2 = m_S^2/(\cos\beta \sin\beta)$, $y_T = 10$ and $0.05 \leq s_L \leq 0.1$. Right: BRs of the H, A states in the 2HDM+VLQ as a function of s_L for the following input parameters: $m_{t'} = 1 \text{ TeV}$, $\sin(\beta - \alpha) = 1$, $m_h = 125.09 \text{ GeV}$, $\tan\beta = 7$, $m_{12}^2 = m_S^2/(\cos\beta \sin\beta)$ and $y_T = 10$.

also $t\bar{t}$, which in fact becomes the dominant one) and (as implied by the previous footnote) that $\text{BR}(A \rightarrow \gamma\gamma)$ is significantly larger than $\text{BR}(A \rightarrow Z\gamma)$.

For the same choice of 2HDM+VLQ parameters as in figure 13, upon fixing $s_L = 0.05$ (left) and $s_L = 0.09$ (right), we present in figure 14 the reaches over the $(m_{t'}, m_S)$ plane for the two adopted luminosities, i.e., end of Run II and Run III⁴. Significances here are most sensitive to the value of $\tan\beta$ and s_L , whereas the other parameters (m_h , m_{H^\pm} , m_{12}^2 and y_T) have little influence, and are such that significant coverage exists in both $m_{t'}$ and, despite the low diphoton BRs past $2m_t$, $m_H = m_A$, up to the kinematic limit of the $t' \rightarrow St$ decay.

6 Conclusions

While the case for VLQs, especially those of top flavour, has already been well established from the theoretical side, the experimental pursuit of their signatures at the LHC has been somewhat limited, as ATLAS and CMS analyses have primarily been carried out under the assumption that such new states of matter decay into SM particles only, i.e., via $t' \rightarrow W^+ b, Zt$ and ht . This approach clearly enables one to make the most in terms of optimising the signal-to-background ratio in an analysis, chiefly because one can attempt reconstructing the measured W^+ , Z and h masses. However, if one considers VLQ models with additional particles this is overly restrictive since the VLQ may decay via exotic channels involving

⁴Notice that the 2HDM+VLQ signal is here computed using an adapted version of 2HDMC [64] for the t' and H/A decays. Further, for the MC analysis, the aforementioned MADGRAPH version was used.

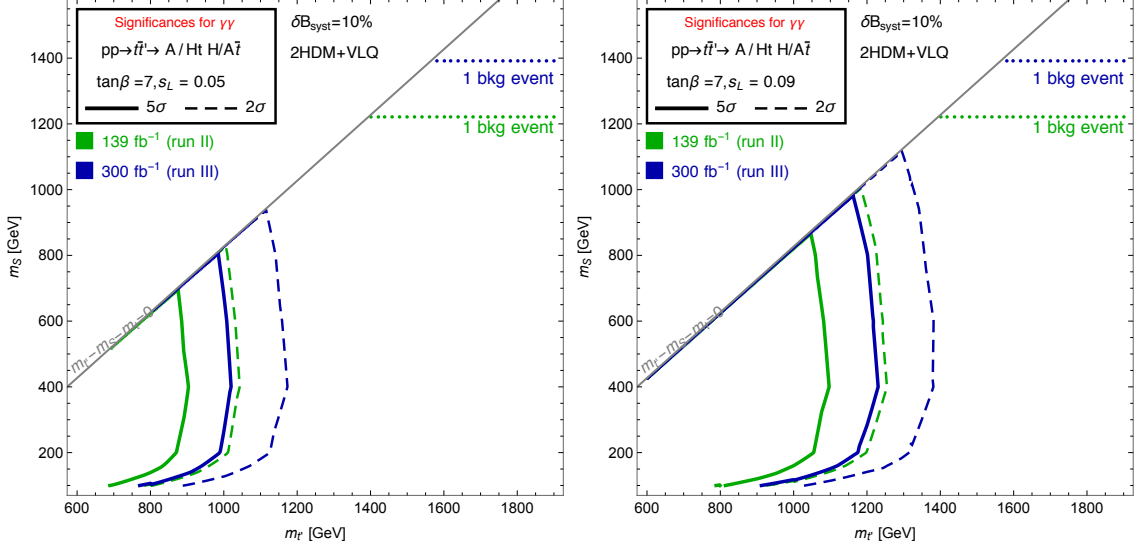


Figure 14: Significances in the 2HDM+VLQ with for the inputs parameters of figure 13 with the exception of and $s_L = 0.05$ (left) and $s_L = 0.09$ (right). The coding colour is the same as in figure 10.

scalars or pseudoscalars. While the kinematic handles available to enhance these exotic channels may be apparently limited in comparison (as the exotic scalar or pseudoscalar states may have not been discovered already and/or their mass not measured), the size of the associated BRs could be large enough so as to nonetheless enable sensitivity to these channels. Furthermore, if the companion Higgs states are heavier than the W^+ , Z and h objects of the SM, the signal would anyhow be present in a region of space where the background contamination is minimised.

Based on this reasoning, in this paper, we have set out to assess the scope of the LHC to test t' decays into neutral (pseudo)scalar states, whose nature could be either fundamental or composite. As an example of spin-0 fundamental states, we have assumed here a Higgs sector comprised of the SM state supplemented by a scalar boson as well as a 2HDM (Type-II) containing both a scalar and pseudoscalar state (which we have taken as degenerate in mass). As an example of spin-0 composite states, we have looked at a CHM where an additional pseudoscalar state emerges as a pNGB of the underlying new strong dynamics. In fact, we have also shown how all such models can conveniently be parametrised in the form of a simplified model onto which they can be mapped.

Of the various possible decay modes of this additional neutral (pseudo)scalar bosons, which we have collectively labelled as S , we have considered here two of the cleanest probes possible at the LHC, i.e., $S \rightarrow \gamma\gamma$ and $Z\gamma$ (with the Z decaying into electron/muon pairs). In doing so, we have performed a dedicated signal-to-background analysis exploiting parton level event generation, QCD shower and hadronisation effects as well as detector emulation aimed at establishing the sensitivity of the LHC experiments to such decays, where the S state emerges from a companion top decay, $t' \rightarrow St$, following $t'\bar{t}'$ production (with the \bar{t}' decay treated inclusively). In the case of both S signatures, we have not attempted

any reconstruction of the SM top quark entering the t' decay chain although, on a trial-and-error basis, we have assumed knowledge of the S mass, to be able to exploit both the cleanliness of the two S decay channels and the ability of a standard LHC detector in sampling $\gamma\gamma$ and $Z(\rightarrow \ell^+\ell^-)\gamma$ invariant masses with high resolution. Indeed, this approach also enables us to compare on a more equal footing the scope of $t' \rightarrow St$ signatures with that of $t' \rightarrow W^+b$, Zt and ht ones, where a mass reconstruction is normally imposed on the W^\pm , Z and h decay products.

As a result of this approach, we have found that the $t' \rightarrow St$ signatures give a level of sensitivity not dissimilar from that obtained through studies of $t' \rightarrow W^+b$, Zt and ht . For specific regions of the parameter space of VLQ models with exotic Higgs states, which have survived all available constraints from both direct and indirect t' and S searches (including those obtained by ourselves from recasting experimental studies for other sectors), we have found the following exclusion and discovery reaches. For a simplified model maximising both the t' and S BRs, $m_{t'}$ can be probed in both the $\gamma\gamma$ and $Z\gamma$ channels up to approximately 2 TeV for S masses well into the TeV region. In the CHM scenario considered, coverage is not dissimilar for the $\gamma\gamma$ case but for the $Z\gamma$ the t' reach is limited to 1.6 TeV. In the 2HDM+VLQ, testable regions in the $(m_{t'}, m_S)$ plane (where S represents a superposition of degenerate H and A states) can extend to 1.2–1.4 TeV for the t' mass and 0.8–1 TeV for the A mass, depending on the choice of the other parameters, albeit limited to the $\gamma\gamma$ case, as $Z\gamma$ gives no sensitivity during both Run II and III.

In summary, we believe that there is significant margin for improving the sensitivity of the LHC to models with a heavy top partner, through the exploitation of its decay channels into exotic (i.e., non-SM-like) neutral (pseudo)scalar states, which are ubiquitous in BSM constructs containing such a new fermion. In fact, over sizeable regions of the parameter space of the realistic VLQ models considered here, we have found that sensitivity to both the t' and S mass can extend well into the TeV region, thereby being competitive with the currently studied SM channels. While in this paper we have limited ourselves to illustrating this through a few benchmark examples, in a forthcoming paper, we shall quantify the regions of parameter space of our models where such a phenomenology can be realised.

A Details of the models

In this appendix, additional details are given of the models; the 2HDM+VLQ model in appendix A.1 and the composite Higgs model in appendix A.2.

A.1 The 2HDM with an additional VLQ

The scalar potential of the model includes two identical scalar doublets (Φ_1, Φ_2) and a discrete symmetry $\Phi_i \rightarrow (-1)^i \Phi_i$ ($i = 1, 2$), which is only violated softly by dimension-two terms [22],

$$V = m_{11}^2 \Phi_1^\dagger \Phi_1 + m_{22}^2 \Phi_2^\dagger \Phi_2 - m_{12}^2 (\Phi_1^\dagger \Phi_2 + \Phi_2^\dagger \Phi_1) + \frac{\lambda_1}{2} (\Phi_1^\dagger \Phi_1)^2 + \frac{\lambda_2}{2} (\Phi_2^\dagger \Phi_2)^2 + \lambda_3 (\Phi_1^\dagger \Phi_1) (\Phi_2^\dagger \Phi_2) + \lambda_4 (\Phi_1^\dagger \Phi_2) (\Phi_2^\dagger \Phi_1) + \frac{\lambda_5}{2} \left[(\Phi_1^\dagger \Phi_2)^2 + (\Phi_2^\dagger \Phi_1)^2 \right]. \quad (\text{A.1})$$

We take all parameters in the above potential to be real (although m_{12}^2 and λ_5 could in principle be complex). The two complex scalar doublets may be rotated into a basis where only one doublet acquires a VEV, the *Higgs basis*,

$$H_1 = \frac{1}{\sqrt{2}} \begin{pmatrix} \sqrt{2} G^+ \\ v + \varphi_1^0 + iG^0 \end{pmatrix}, \quad H_2 = \frac{1}{\sqrt{2}} \begin{pmatrix} \sqrt{2} H^+ \\ \varphi_2^0 + iA \end{pmatrix}, \quad (\text{A.2})$$

where G^0 and G^\pm are the would-be Goldstone bosons and H^\pm are a pair of charged Higgs bosons. A is the CP odd pseudoscalar, which does not mix with the other neutral states. The Goldstone bosons are aligned with the VEV in Higgs flavor space, while the A is orthogonal. The physical CP even scalars h and H are mixtures of $\varphi_{1,2}^0$ and the scalar mixing is parametrized as

$$\begin{pmatrix} h \\ H \end{pmatrix} = \begin{pmatrix} s_{\beta-\alpha} & c_{\beta-\alpha} \\ c_{\beta-\alpha} & -s_{\beta-\alpha} \end{pmatrix} \begin{pmatrix} \varphi_1^0 \\ \varphi_2^0 \end{pmatrix}, \quad (\text{A.3})$$

where $\tan \beta = v_1/v_2$ is the angle used to rotate $\Phi_{1,2}$ to the Higgs basis fields $H_{1,2}$, α is the additional mixing angle needed to diagonalize the mass matrix of the CP-even scalars, and $s_{\beta-\alpha} = \sin(\beta - \alpha)$, $c_{\beta-\alpha} = \cos(\beta - \alpha)$. The most general renormalisable interaction and mass terms involving the VLQ can be described by the following Lagrangian (where we only include the third generation SM quarks),

$$- \mathcal{L}_Y \supset y_T \bar{Q}_L \tilde{H}_2 T_R + \xi_T \bar{Q}_L \tilde{H}_1 T_R + M \bar{T}_L T_R, \quad (\text{A.4})$$

where $\tilde{H}_i \equiv i\sigma_2 H_i^*$ ($i = 1, 2$), Q_L is the SM quark doublet and M is a bare mass term for the VLQ, which is unrelated to the Higgs mechanism of EWSB. Note that often the Yukawa couplings of the 2HDM are written in terms of the fields Φ_1, Φ_2 . In eq. (A.4) we use the Higgs basis fields, so the Yukawa couplings y_T, ξ_T must be defined accordingly. In a Type II-model, as we are considering in this paper, the up-type quarks only couple to the doublet Φ_2 , while down-type quarks only couple to Φ_1 . Additional mixing terms of the form $\bar{T}_L t_R$ can always be rotated away and reabsorbed into the definitions of the Yukawa

couplings. In the weak eigenstate basis (\tilde{t}, T) , where \tilde{t} is the SM top quark, the top quark and VLQ mass matrix is

$$\mathcal{M} = \begin{pmatrix} \frac{y_t v}{\sqrt{2}} & \frac{\xi_T v}{\sqrt{2}} \\ 0 & M \end{pmatrix}, \quad (\text{A.5})$$

where y_t is the Yukawa coupling of the top quark. It is clear from the above mass matrix that the physical mass of the heavy top, $m_{t'}$, is different from M due to the t - T mixing. The mass matrix \mathcal{M} can be diagonalised by a bi-unitary transformation in the same way as in section 2.1 to obtain the physical states $(t_{L,R}, t'_{L,R})$ in terms of the gauge eigenstates $(\tilde{t}_{L,R}, T_{L,R})$,

$$\begin{pmatrix} t_{L,R} \\ t'_{L,R} \end{pmatrix} = \begin{pmatrix} c_{L,R} & -s_{L,R} \\ s_{L,R} & c_{L,R} \end{pmatrix} \begin{pmatrix} \tilde{t}_{L,R} \\ T_{L,R} \end{pmatrix} = U_{L,R} \begin{pmatrix} \tilde{t}_{L,R} \\ T_{L,R} \end{pmatrix} \quad (\text{A.6})$$

The mixing angles θ_L and θ_R are not independent parameters. From the bi-unitary transformations we can derive the relations

$$\tan(2\theta_L) = \frac{\sqrt{2}Mv\xi_T}{M^2 - \frac{y_t^2 v^2}{2} - \frac{\xi_T^2 v^2}{2}}, \quad \tan(2\theta_R) = \frac{y_t \xi_T v^2}{M^2 - \frac{y_t^2 v^2}{2} + \frac{\xi_T^2 v^2}{2}}, \quad (\text{A.7})$$

and by using the traces and determinants

$$\text{Tr} \left(U_L \mathcal{M} \mathcal{M}^\dagger U_L^\dagger \right) = m_{t'}^2 + m_t^2 \quad (\text{A.8})$$

$$\det \left(U_L \mathcal{M} \mathcal{M}^\dagger U_L^\dagger \right) = m_t^2 m_{t'}^2 \quad (\text{A.9})$$

we end up with the relations

$$m_{t'}^2 + m_t^2 = M^2 + \frac{y_t^2 v^2}{2} + \frac{\xi_T^2 v^2}{2} \quad (\text{A.10})$$

$$\frac{y_t^2 v^2 M^2}{2} = m_t^2 m_{t'}^2 \quad (\text{A.11})$$

$$M^2 = m_t^2 \sin^2 \theta_L + m_{t'}^2 \cos^2 \theta_L, \quad (\text{A.12})$$

and a relationship between θ_L and θ_R and the Yukawa couplings,

$$\tan \theta_L = \frac{m_t}{m_{t'}} \tan \theta_R, \quad \frac{\xi_T}{y_t} = s_L c_L \frac{m_{t'}^2 - m_t^2}{m_t m_{t'}}. \quad (\text{A.13})$$

The t' - t interaction can thus be described by three independent physical parameters: two quark masses $m_t, m_{t'}$ and a mixing angle $s_L = \sin \theta_L$.

After rotating the weak eigenstates (\tilde{t}_L, T_L) into the mass eigenstates, the Yukawa Lagrangian takes the following form [25]:

$$\begin{aligned} -\mathcal{L}_Y \supset & \frac{1}{\sqrt{2}} (\bar{t}_L, \bar{t}'_L) U_L \left[\varphi_1^0 \begin{pmatrix} y_t & \xi_T \\ 0 & 0 \end{pmatrix} + \varphi_2^0 \begin{pmatrix} y_t \cot \beta & y_T \\ 0 & 0 \end{pmatrix} \right] U_R^\dagger \begin{pmatrix} t_R \\ t'_R \end{pmatrix} \\ & - i (\bar{t}_L, \bar{t}'_L) U_L A \begin{pmatrix} y_t \cot \beta & y_T \\ 0 & 0 \end{pmatrix} U_R^\dagger \begin{pmatrix} t_R \\ t'_R \end{pmatrix}, \end{aligned} \quad (\text{A.14})$$

where $U_{L,R}$ are the matrices appearing in eq. (A.6). In the alignment limit of 2HDM, $\sin(\beta - \alpha) \rightarrow 1$, where the lightest neutral scalar h is the SM-like Higgs boson, the neutral Higgs couplings to top (t) and top partner (t') pairs are in the notation of eq. (2.1) given by (with $S = H$ or A)

$$\begin{aligned}
\kappa_t^H &= -\frac{c_L c_R}{\tan \beta} + \frac{c_L s_R y_T}{y_t} \\
\kappa_{t'}^H &= -\frac{s_L s_R}{\tan \beta} - \frac{s_L c_R y_T}{y_t} \\
\kappa_L^H &= -\frac{c_L s_R}{\tan \beta} - \frac{c_L c_R y_T}{y_t} \\
\kappa_R^H &= -\frac{c_R s_L}{\tan \beta} + \frac{s_L s_R y_T}{y_t} \\
\tilde{\kappa}_t^A &= \frac{c_L c_R}{\tan \beta} - \frac{c_L s_R y_T}{y_t} \\
\tilde{\kappa}_{t'}^A &= \frac{s_L s_R}{\tan \beta} + \frac{s_L c_R y_T}{y_t} \\
-i\kappa_L^A &= \frac{c_L s_R}{\tan \beta} + \frac{c_L c_R y_T}{y_t} \\
-i\kappa_R^A &= \frac{s_L c_R}{\tan \beta} - \frac{s_L s_R y_T}{y_t}.
\end{aligned} \tag{A.15}$$

The couplings here are normalised to $y_t/\sqrt{2}$, which is what the $H_{\text{SM}} t \bar{t}$ coupling would be in the alignment limit and in case of no mixing between the \tilde{t} and T . Note that in eq. (2.1) the terms with diagonal couplings $S t' \bar{t}'$ of the top partner to the scalars are not included, since they are not phenomenologically relevant in this paper. We include them here for completeness, however.

In our analysis we impose various theoretical and experimental constraints on the parameter space of 2HDM+VLQ. We require perturbativity of the involved quartic couplings by setting $|\lambda_i| \leq 4\pi$, and positivity of the potential leads to the conditions

$$\lambda_{1,2} > 0, \quad \text{and} \quad \lambda_3 + \lambda_4 - |\lambda_5| + \sqrt{\lambda_1 \lambda_2} > 0, \quad \text{and} \quad \lambda_3 + \sqrt{\lambda_1 \lambda_2} > 0. \tag{A.16}$$

Finally, for tree-level unitarity of the scattering of Higgs bosons and gauge bosons, we apply the sufficient conditions on the S -matrix given in [65]. In addition, the parameter space is partially constrained by Higgs data from Run II at the LHC, for which we use the latest versions of the public codes HIGGSBOUNDS [66] and HIGGSIGNALS [67].

A.2 The composite Higgs model

As mentioned in the main text, the SM Higgs \mathcal{H} field in this model is a bi-doublet of $\text{SU}(2)_L \times \text{SU}(2)_R$, which together with a singlet S forms the five dimensional anti-symmetric irrep of $\text{Sp}(4)$,

$$\mathcal{H} \oplus S \equiv \begin{pmatrix} H^{0*} & H^+ \\ -H^{+*} & H^0 \end{pmatrix} \oplus S \in (\mathbf{2}, \mathbf{2}) \oplus (\mathbf{1}, \mathbf{1}) = \mathbf{5}. \tag{A.17}$$

The fermionic sector also consists of a bi-doublet and a singlet in the $\mathbf{5}$ of $\text{Sp}(4)$,

$$\Psi \equiv \begin{pmatrix} T & X \\ B & T' \end{pmatrix} \oplus \tilde{T} \in (\mathbf{2}, \mathbf{2}) \oplus (\mathbf{1}, \mathbf{1}) = \mathbf{5}. \tag{A.18}$$

The new fermions mix with the third family quarks of the SM. The mixing is obtained by choosing to embed both the left-handed $Q_L = (\tilde{t}_L, b_L)^T$ and the right-handed \tilde{t}_R as spurions into the $\mathbf{6}$ of $SU(4)$. The non-zero components of Q_L fit into the bi-doublet of the $SU(2)_L \times SU(2)_R$ subgroup, while \tilde{t}_R is in the singlet of the $\mathbf{6} \rightarrow \mathbf{5} + \mathbf{1}$ decomposition of $SU(4) \rightarrow Sp(4)$. The choice for Q_L is essentially dictated by the need to preserve the custodial symmetry of [32].

The construction of the interaction Lagrangian from the general formalism has been addressed in many papers and will not be reviewed here. Suffice it to say that we combine the five pNGBs into a 4×4 matrix Π and exponentiate it to obtain

$$\Sigma = \exp\left(\frac{i\sqrt{2}}{f}\Pi\right), \text{ transforming as: } \Sigma \rightarrow g\Sigma h^{-1}, \text{ for } g \in SU(4), h \in Sp(4), \quad (\text{A.19})$$

and use it to “dress” the fermionic field Ψ , written as a 4×4 anti-symmetric matrix. In this notation, the Lagrangian becomes

$$\mathcal{L} = y_L f \text{tr}(\bar{Q}_L \Sigma \Psi_R \Sigma^T) + y_R f \text{tr}(\Sigma^* \bar{\Psi}_L \Sigma^\dagger \tilde{t}_R) - M \text{tr}(\bar{\Psi}_L \Psi_R) + \text{h.c.} \quad (\text{A.20})$$

where we indicated the dressing explicitly. (Note that $Q_L \rightarrow gQ_L g^T$ and $\Psi \rightarrow h\Psi h^T$.)

We allow only the Higgs field to acquire a VEV, and we denote the mixing angle by $\sin \theta = v/f$, where $v = 246$ GeV. Generically $f > 800$ GeV from EWPT, although one can envisage mechanisms that would allow to lower that bound [68].

Computing eq. (A.20) to all orders in θ and retaining only terms linear in h and S , h being the canonically normalised physical Higgs with VEV shifted to zero, we can write the part of eq. (A.20) concerning top partners as (see also [21])

$$\mathcal{L}_{\text{tops}} = - \begin{pmatrix} \tilde{t}_L & \bar{T}_L & \bar{T}'_L & \tilde{T}_L \end{pmatrix} \left(\mathcal{M} + h\mathcal{I}_h + S\mathcal{I}_S \right) \begin{pmatrix} \tilde{t}_R \\ T_R \\ T'_R \\ \tilde{T}_R \end{pmatrix} + \text{h.c.} \quad (\text{A.21})$$

where the mass and Yukawa matrices are given by

$$\begin{aligned}
\mathcal{M} &= \begin{pmatrix} 0 & y_L f \cos^2(\frac{\theta}{2}) & -y_L f \sin^2(\frac{\theta}{2}) & 0 \\ \frac{y_R f}{\sqrt{2}} \sin \theta & M & 0 & 0 \\ \frac{y_R f}{\sqrt{2}} \sin \theta & 0 & M & 0 \\ 0 & 0 & 0 & M \end{pmatrix} \\
\mathcal{I}_h &= \begin{pmatrix} 0 & -\frac{1}{2}y_L \sin \theta & -\frac{1}{2}y_L \sin \theta & 0 \\ \frac{y_R}{\sqrt{2}} \cos \theta & 0 & 0 & 0 \\ \frac{y_R}{\sqrt{2}} \cos \theta & 0 & 0 & 0 \\ 0 & 0 & 0 & 0 \end{pmatrix} \\
\mathcal{I}_S &= \begin{pmatrix} 0 & 0 & 0 & \frac{iy_L}{\sqrt{2}} \sin \theta \\ 0 & 0 & 0 & 0 \\ 0 & 0 & 0 & 0 \\ iy_R \cos \theta & 0 & 0 & 0 \end{pmatrix}.
\end{aligned} \tag{A.22}$$

The singular value decomposition of \mathcal{M} is unwieldy, but can be performed numerically or perturbatively to order $\theta \approx v/f$. For the four top quark mass eigenstates t, t', t'', t''' , the perturbative expressions for the masses are

$$m_t = \frac{y_L y_R f v}{\sqrt{2} \widehat{M}} + \mathcal{O}\left(\frac{v^2}{f^2}\right), \quad m_{t'} = M, \quad m_{t''} = M + \mathcal{O}\left(\frac{v^2}{f^2}\right), \quad m_{t'''} = \widehat{M} + \mathcal{O}\left(\frac{v^2}{f^2}\right). \tag{A.23}$$

The mass of the bottom partner (mostly aligned with B) turns out to be of the same order as that of the heaviest top partner $m_{t''}$, while X has mass equal to $M \equiv m_{t'}$ since it does not mix with anything. For the top quarks, the conversion from gauge to mass eigenbasis reads, to $\mathcal{O}(v/f)$,

$$\begin{aligned}
\tilde{t}_L &= -\frac{M}{\widehat{M}} t_L + \frac{y_L f}{\widehat{M}} t_L''', \quad T_L = \frac{y_L f}{\widehat{M}} t_L + \frac{M}{\widehat{M}} t_L''', \quad T'_L = t_L'', \quad \tilde{T}_L = t'_L \\
\tilde{t}_R &= t_R + \frac{y_R v}{\sqrt{2} M} t_R'' + \frac{y_R v M}{\sqrt{2} \widehat{M}^2} t_R''', \quad T_R = t_R''' - \frac{y_R v M}{\sqrt{2} \widehat{M}^2} t_R, \quad T'_R = t_R'' - \frac{y_R v}{\sqrt{2} M} t_R, \quad \tilde{T}_R = t'_R.
\end{aligned} \tag{A.24}$$

This spectrum justifies that choice of simplified model in the text where we neglect all the top partners other than the lightest one.

Regarding decays of the pseudoscalar in this model, in figure 15 we show the partial widths of S as a function of its mass, including the dominant loop induced fermionic channel $S \rightarrow \bar{b}b$ relevant below the $Z\gamma$ threshold. We use $f/(A \cos \theta) = 500$ GeV but all curves rescale by $(500 \text{ GeV } A \cos \theta / f)^2$. We see that for all interesting regions of parameters the width is always very narrow, but still prompt.

The most promising parameter region for this class of models is $m_S \lesssim 160$ GeV, where the S decays dominantly to $Z\gamma$. This region is motivated from the model building perspective since it is expected $m_S < m_h$. From the experimental point of view it offers

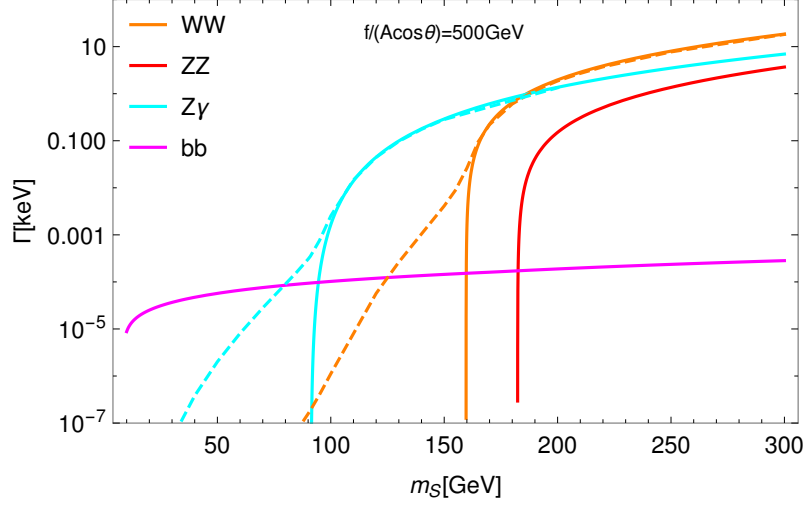


Figure 15: Partial width of S in the dominant decay channels for the composite Higgs model benchmark scenario discussed in section 2.3. The dashed lines denote the contribution with at least one off-shell weak boson.

a clear benchmark of a $Z\gamma$ channel. Above $2m_W$ the WW channel overcomes, and for $m_S \lesssim 80$ GeV the $b\bar{b}$ channel dominates, both of which are less clean channels experimentally.

B Range of validity of the analysis

In this appendix, two aspects of the range validity of the analysis is discussed: the difference between a scalar or pseudoscalar S boson in appendix B.1 and the validity of the narrow-width approximation in appendix B.2.

B.1 Distinguishing the dominant chirality of t' coupling and the scalar or pseudoscalar nature of S

If an observation is made in the final states considered in this analysis, it will be very relevant to characterise the properties of the particles responsible for the excess. Among such properties, we focus here on distinguishing if the dominant chirality of the VLQ is left or right and whether the spin-0 boson is a scalar or a pseudoscalar. For this purpose we will consider differences in shapes for relevant kinematical observables, and in this section we will provide examples of distributions for different mass configurations in the $m_{t'}$ vs m_S plane for the channels considered in this analysis.

It is known that the dominant chirality of the couplings of a VLQ interacting with the SM top quark can be probed by looking at the transverse momentum of the decay products of the W boson emerging from the top quark [69, 70]. Differently from the SM case, however, here the kinematics of the decay products of t' is not only affected by its mass, but also by the S mass. The scalar or pseudoscalar nature of S can also affect the kinematical distributions of its decay products. We have therefore performed simulations imposing specific decay channels, to check, at reconstruction level but without including detector effects, how large differences can be between the above scenarios in differential distributions.

For the $\gamma\gamma$ decay of S the only distributions which can probe its scalar/pseudoscalar nature are those related to the photons. To verify the coupling chirality we have then imposed the following chains for the top and anti-top branches: $t \rightarrow W^+b \rightarrow e^+\nu_e b$ and $\bar{t} \rightarrow W^-\bar{b} \rightarrow \mu^-\bar{\nu}_\mu \bar{b}$. Representative distributions for this channel are shown in figure 16 for two different mass configurations of t' and S : $m_{t'} = 1$ TeV and $m_S = 300$ GeV or 800 GeV, i.e. for large and small mass splitting.

The distribution of the leptons emerging from top chain decay (left panels) show that in principle a distinction between the dominant chiralities is easier for large mass splittings, while for small mass splittings the differences are much less pronounced. The inclusion of all decay channels and detector effects will reduce differences even more, such that a distinction between different chiralities is not generally easily doable. For this reason, in this analysis we will focus only on interactions where the SM top quark is right-handed.

Considering the separation between photons for scalar/pseudoscalar characterisation, no differences can be observed in the two mass splitting cases. In both mass splitting scenarios we have considered the separation between the leading and third photon (in p_T ordering) as statistically the second photon is more likely to be originated by the other S , given the symmetry of the process. We have verified that no sizeable differences can be seen in any other distribution related to the photons, including transverse momenta, pseudorapidities and separations between different photons. Hence, the scalar/pseudoscalar

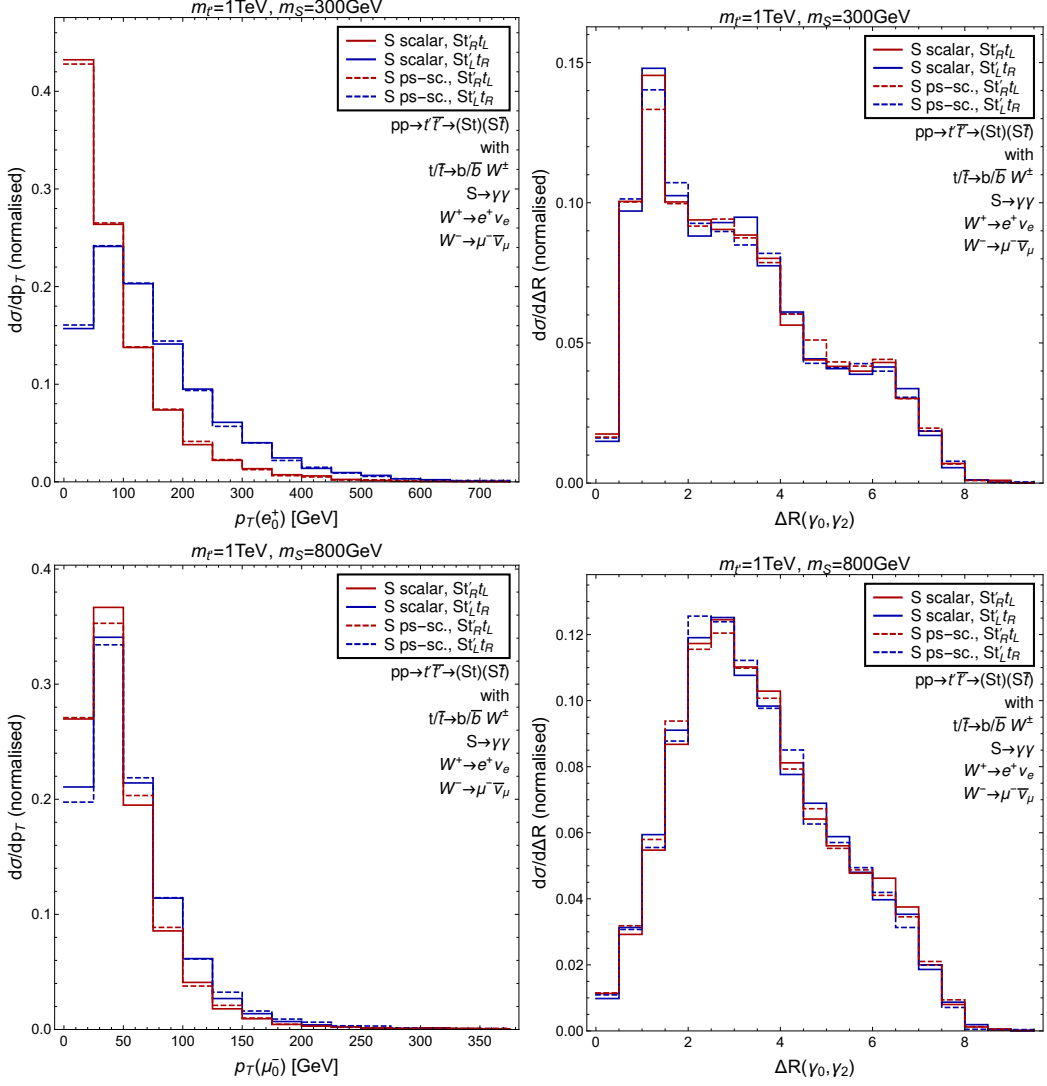


Figure 16: Representative distributions for chirality and scalar/pseudoscalar discrimination in the $\gamma\gamma$ channel. Top-left: transverse momentum of the leading positron. Bottom-left: transverse momentum of the leading muon. Right panels: separation between leading and second photon. The top panels correspond to a scenario with large mass splitting between t' and S while the bottom panels correspond to a small mass splitting scenario. In all panels, different line colours correspond to different coupling chiralities, while different line styles correspond to scalar or pseudoscalar hypotheses.

nature of S cannot be characterised through a kinematical description of the final state for this channel, and results can be interpreted in both scenarios.

For the $Z\gamma$ decay of S we have imposed a fully hadronic decay for the top and anti-top but we have distinguished the decays of the two Z bosons by imposing that one decays to electrons and the other to muons in order to separate the information coming from different branches. In figure 17 representative distributions are shown for analogous mass

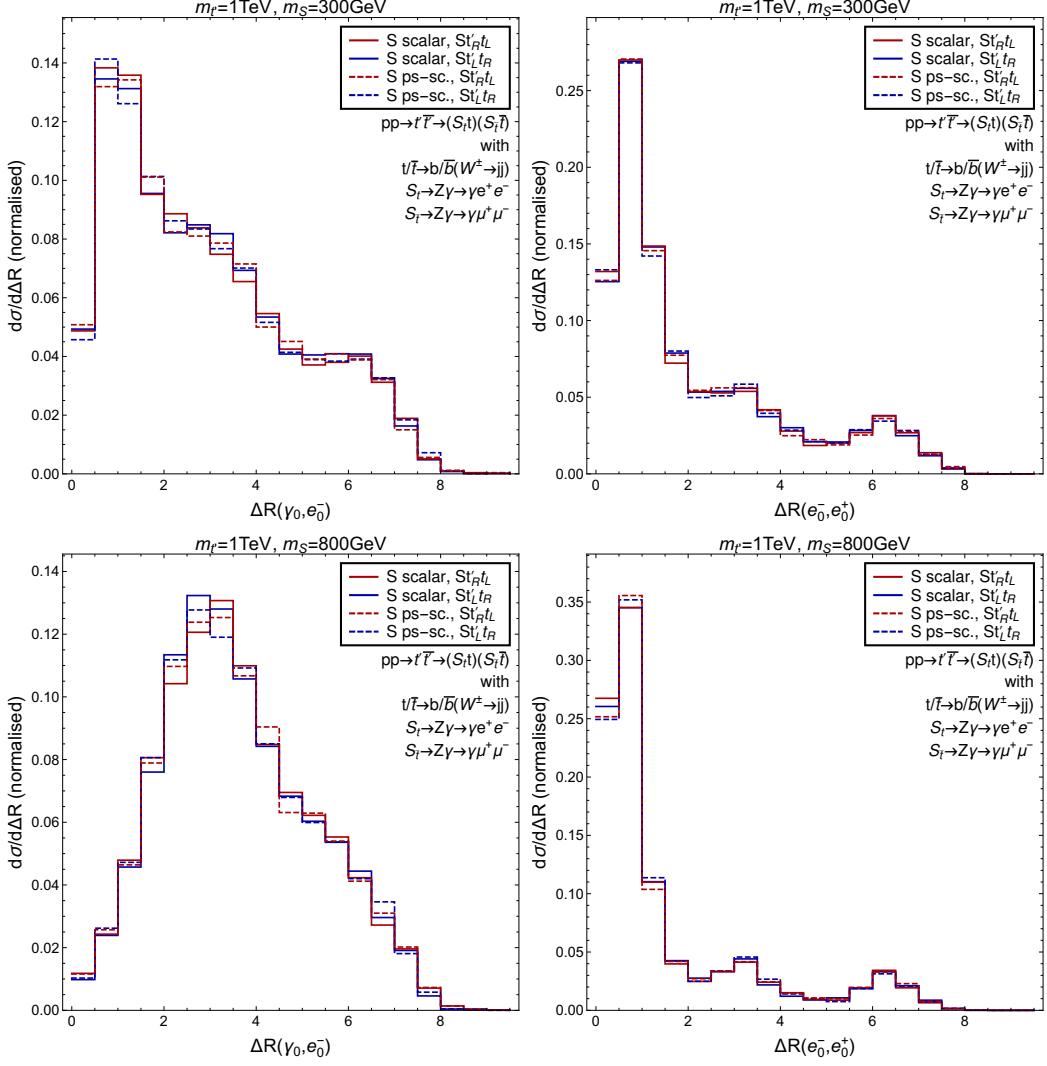


Figure 17: Representative distributions for chirality and scalar/pseudoscalar discrimination in the $Z\gamma$ channel. Left panels: separation between leading photon and leading electron. Right panels: separation between leading electron and positron. The top panels correspond to a scenario with large mass splitting between t' and S while the bottom panels correspond to a small mass splitting scenario. In all panels, different line colours correspond to different coupling chiralities, while different line styles correspond to scalar or pseudoscalar hypotheses.

configurations as in the $\gamma\gamma$ case. The separation between the electron emitted by the Z and the photon and the separation between the electron and positron emitted by the Z are considered. Both distributions exhibit the absence of differences between scalar or pseudoscalar scenarios. Other distributions involving kinematical properties of decay products of S do not show relevant features, and therefore, also for the $Z\gamma$ channel a discrimination between scalar and pseudoscalar cases is not possible.

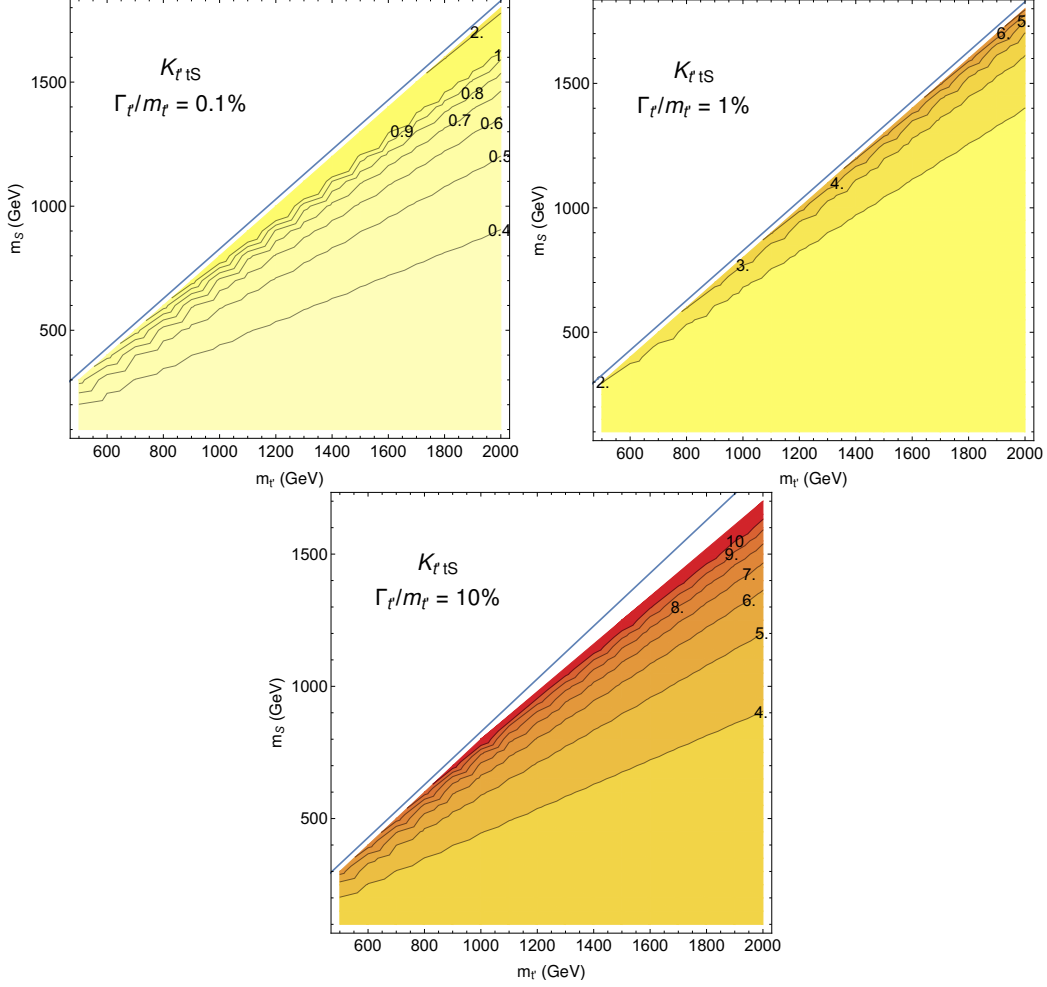


Figure 18: Values of the $\kappa_{L,R}^S$ coupling corresponding to fixed $\Gamma_{t'}/m_{t'}$ ratios (0.1%, 1% and 10%) in the $\{m_{t'}, m_S\}$ plane. The blue contour corresponds to the kinematic limit $m_{t'} - m_t - m_S = 0$. The maximum value for the coupling to be in the perturbative region has been limited to 4π .

B.2 Validity of the narrow-width approximation

In the processes under consideration both t' and S are assumed to be in the narrow-width approximation (NWA), in order to factorise the production of the top partner from its decay chain. Such assumption, however, implies that the coupling $t'tS$ cannot exceed specific values which depend on the masses of t' and S according to the relation in eq. (2.2). Considering as a simplifying and extreme assumption that the only available decay channel for t' is into the SM top and S and that one chirality of the couplings is dominant with respect to the other, such that either $\kappa_R^S \ll \kappa_L^S$ or vice versa, the values of the coupling corresponding to different $\Gamma_{t'}/m_{t'}$ ratios is shown in figure 18. For a specific $\{m_{t'}, m_S\}$ configuration, values of the coupling larger than those in the contours of figure 18 would produce a larger width. The determination of the validity of the NWA approximation

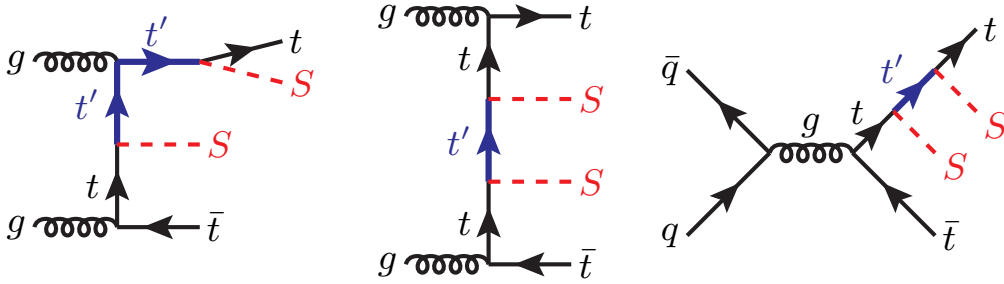


Figure 19: Examples of topologies containing at least one t' propagator and leading to the same final state for the process $pp \rightarrow t\bar{t}SS$.

is important to understand the reliability of the results. If the t' width is not narrow, off-shellness effects in the process of pair production and the contribution from topologies which are neglected in the NWA, represented by the examples of figure 19, can become more and more relevant.

To assess how the width of t' affects the determination of the cross-section, the full $2 \rightarrow 4$ process $pp \rightarrow t\bar{t}SS$ has been evaluated by imposing the presence of at least one t' propagator in the topologies, in order to obtain the signal under the assumption of negligible $S\bar{t}t$ coupling. With such process, the off-shellness effects and contribution of topologies such as those in figure 19 are fully taken into account. Still under the assumption that t' can only decay to $S\bar{t}$ and therefore that the only way to increase the total width of t' for a given $\{m_{t'}, m_S\}$ configuration is by increasing $\kappa_{L,R}^S$, the ratio between the cross-sections of the full process and of the pair-production process in the NWA is shown in figure 20.

The effect of a large width is already noticeable when the $\Gamma_{t'}/m_{t'}$ ratio reaches 1%, when the interference between the resonant channels and all the other contributions is negative and of the order of few percents in a region where $m_S + m_t$ is around 80% of $m_{t'}$. If the $\Gamma_{t'}/m_{t'}$ ratio is below 1% the relative ratio between cross-sections is dominated by the statistical fluctuations of the simulation. For this reason, the numerical results in the following sections assume $\Gamma_{t'}/m_{t'}$ to be of order 0.1%.

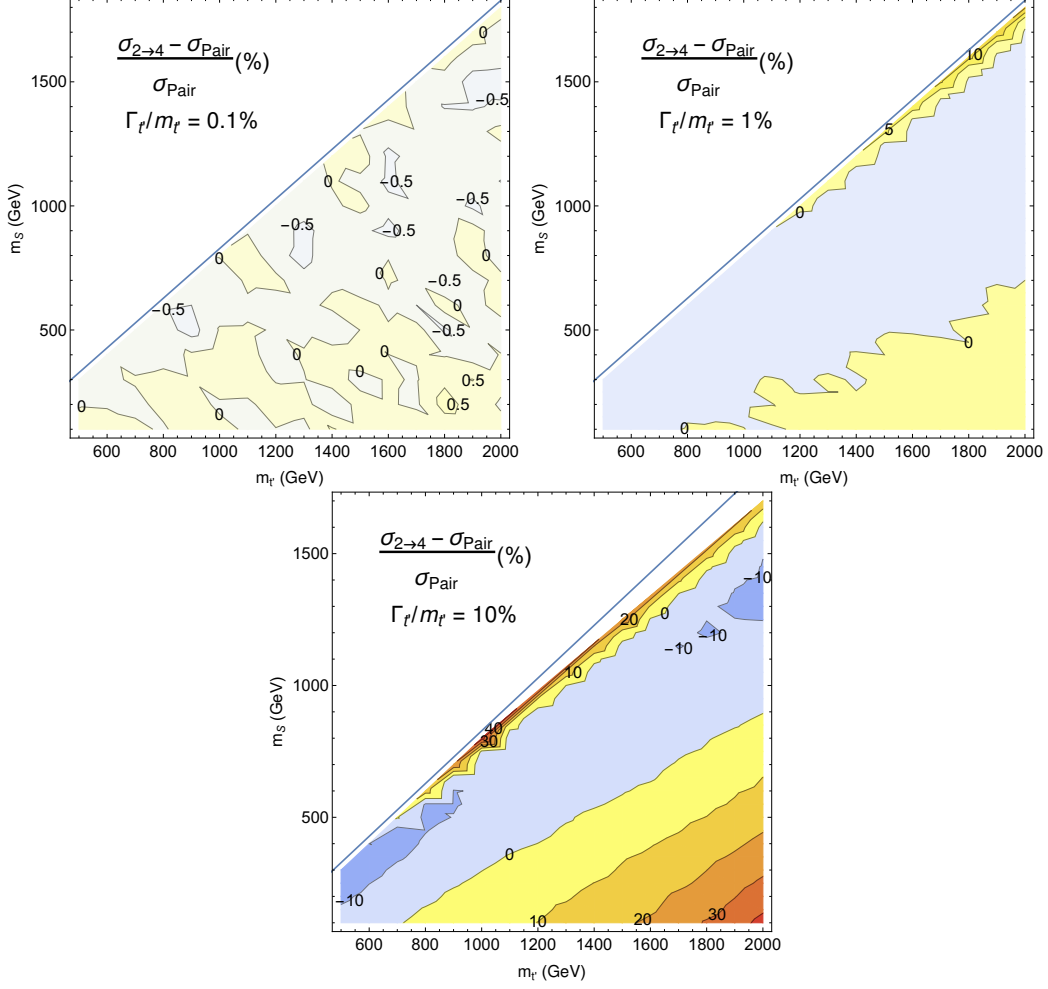


Figure 20: Relative ratio of the cross-sections for the full process $pp \rightarrow t\bar{t}SS$ ($\sigma_{2 \rightarrow 4}$) and for the pair production process $pp \rightarrow t'\bar{t}' \rightarrow (St)(S\bar{t})$ where the t' production and decay are factorised in the NWA approximation (σ_{Pair}). The ratio is shown for different values of the $\Gamma_{t'}/m_{t'}$ ratios (0.1%, 1% and 10%), and the couplings $\kappa_{L,R}^S$ are not allowed to exceed the perturbative limit 4π .

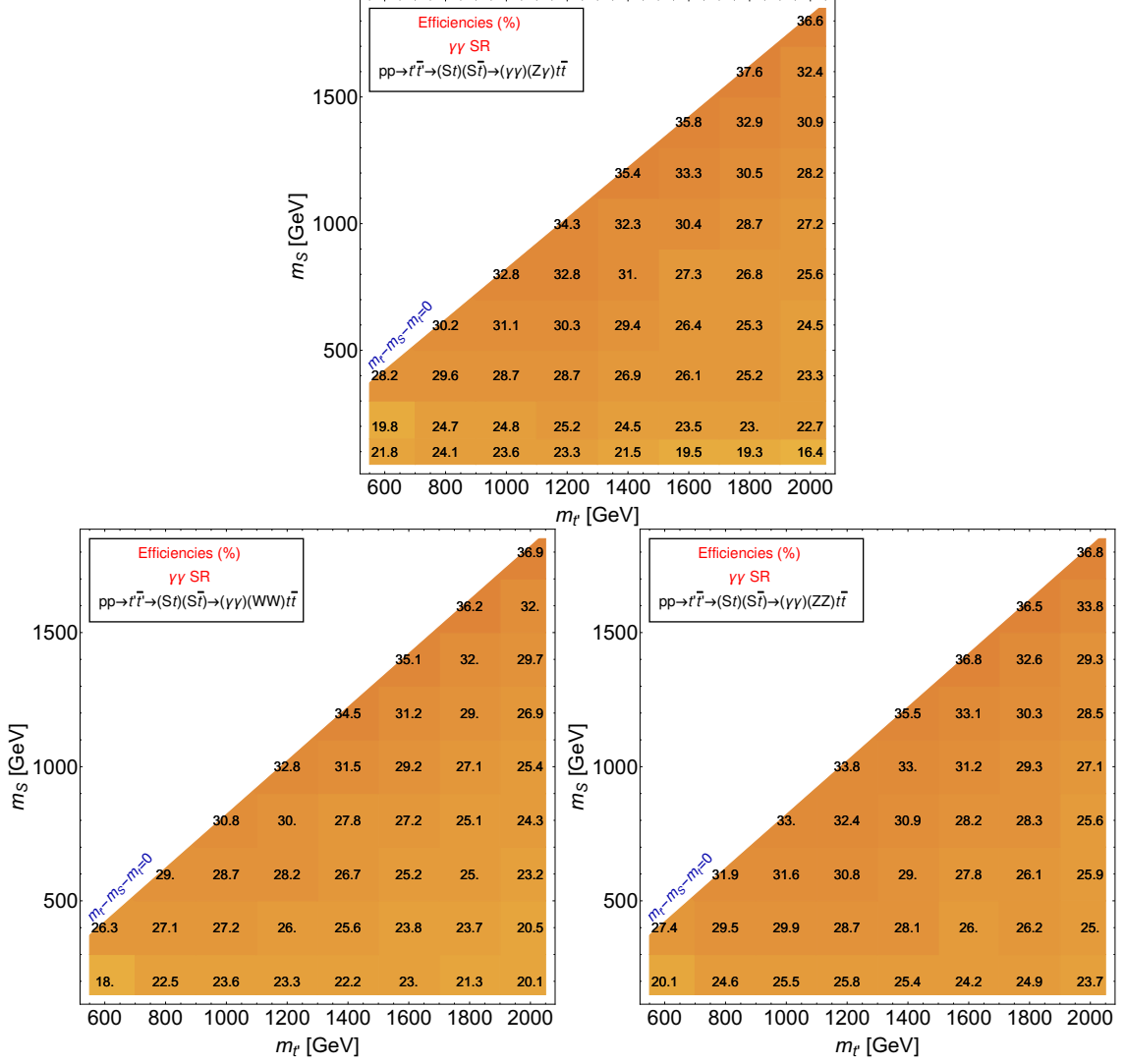


Figure 21: Efficiencies for the $\gamma\gamma$ SR and for channels where at least one of the two S decays into $\gamma\gamma$.

C Signal efficiencies

In this appendix we present the signal efficiencies for each channel and mass point considered in the analysis, except those already shown in figure 9. Figures 21, 22, 23 and 24 show, respectively, the efficiencies for the $\gamma\gamma$ SR and for channels where at least one of the two S decays into $\gamma\gamma$, $\gamma\gamma$ SR and at least one S decaying to $Z\gamma$, $Z\gamma$ SR and at least one S decaying to $\gamma\gamma$ and $Z\gamma$ SR and at least one S decaying to $Z\gamma$.

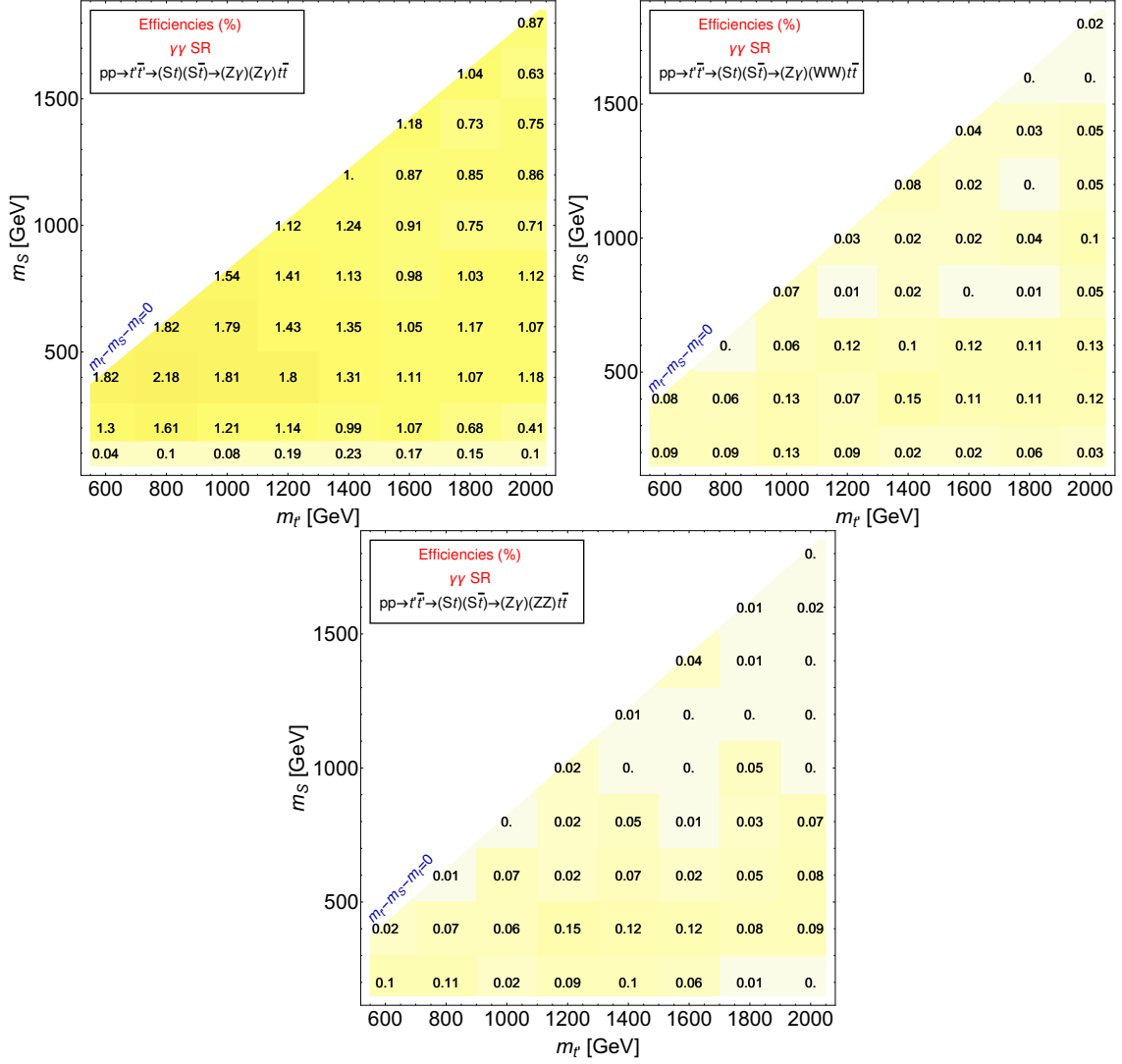


Figure 22: Efficiencies for the $\gamma\gamma$ SR and for channels where at least one of the two S decays into $Z\gamma$.

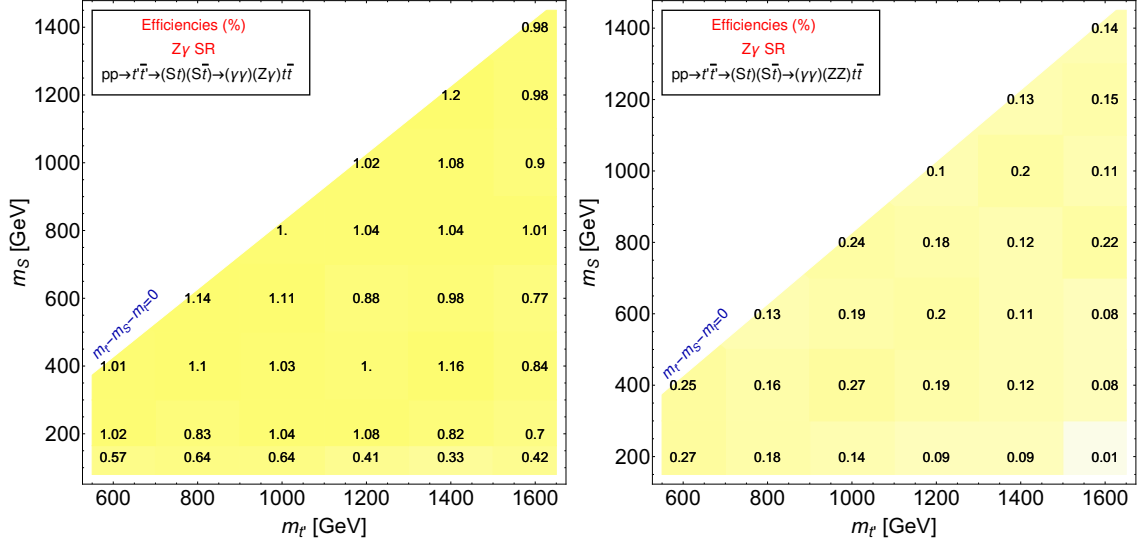


Figure 23: Efficiencies for the $Z\gamma$ SR and for channels where at least one of the two S decays into $\gamma\gamma$.

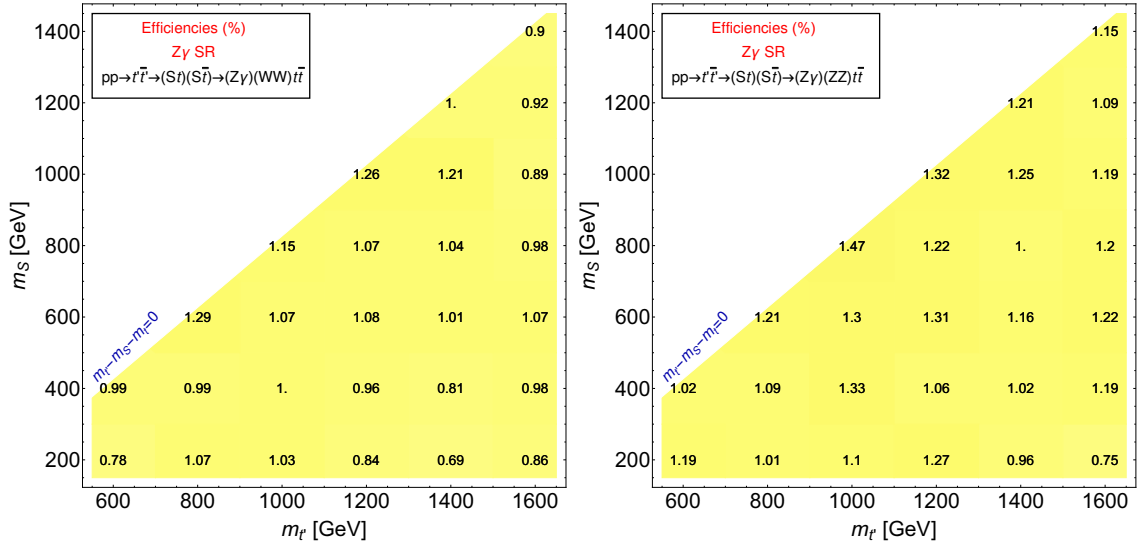


Figure 24: Efficiencies for the $Z\gamma$ SR and for channels where at least one of the two S decays into $Z\gamma$.

Acknowledgments

This work would not have been possible without financing from the Knut and Alice Wallenberg foundation under the grant KAW 2017.0100, which supported EBK, DBF, VE, RE, GF, T.Mathisen and LP as a part of the SHIFT project. RB's work is supported by the Moroccan Ministry of Higher Education and Scientific Research MESRSFC and CNRST: Project PPR/2015/6. RB, RE and SM are supported in part by the H2020-MSCA-RISE-2014 grant agreement No. 645722 (NonMinimalHiggs). T.Mandal is grateful for support from The Royal Society of Arts and Sciences of Uppsala. Y-BL is supported by the Foundation of Henan Institute of Science and Technology (Grant no. 2016ZD01) and the China Scholarship Council (201708410324). SM is supported in part by the NExT Institute and the STFC Consolidated Grant ST/L000296/1. DBF would like to thank the ITP of the Göttingen University and GWDG for providing computing resources. MI wishes to thank the Swedish National Infrastructure for Computing (project SNIC 2019/3-68) for computing resources. LP and Y-BL acknowledge the use of the IRIDIS HPC Facility at the University of Southampton.

References

- [1] O. Eberhardt, G. Herbert, H. Lacker, A. Lenz, A. Menzel, U. Nierste et al., *Impact of a Higgs boson at a mass of 126 GeV on the standard model with three and four fermion generations*, *Phys. Rev. Lett.* **109** (2012) 241802, [[1209.1101](#)].
- [2] M. Buchkremer, G. Cacciapaglia, A. Deandrea and L. Panizzi, *Model Independent Framework for Searches of Top Partners*, *Nucl. Phys.* **B876** (2013) 376–417, [[1305.4172](#)].
- [3] J. A. Aguilar-Saavedra, R. Benbrik, S. Heinemeyer and M. Pérez-Victoria, *Handbook of vectorlike quarks: Mixing and single production*, *Phys. Rev.* **D88** (2013) 094010, [[1306.0572](#)].
- [4] ATLAS collaboration, M. Aaboud et al., *Combination of the searches for pair-produced vector-like partners of the third-generation quarks at $\sqrt{s} = 13$ TeV with the ATLAS detector*, *Phys. Rev. Lett.* **121** (2018) 211801, [[1808.02343](#)].
- [5] ATLAS collaboration, M. Aaboud et al., *Search for pair production of heavy vector-like quarks decaying into hadronic final states in pp collisions at $\sqrt{s} = 13$ TeV with the ATLAS detector*, *Phys. Rev.* **D98** (2018) 092005, [[1808.01771](#)].
- [6] ATLAS collaboration, M. Aaboud et al., *Search for new phenomena in events with same-charge leptons and b-jets in pp collisions at $\sqrt{s} = 13$ TeV with the ATLAS detector*, *JHEP* **12** (2018) 039, [[1807.11883](#)].
- [7] ATLAS collaboration, M. Aaboud et al., *Search for pair production of heavy vector-like quarks decaying into high- p_T W bosons and top quarks in the lepton-plus-jets final state in pp collisions at $\sqrt{s} = 13$ TeV with the ATLAS detector*, *JHEP* **08** (2018) 048, [[1806.01762](#)].
- [8] ATLAS collaboration, M. Aaboud et al., *Search for pair- and single-production of vector-like quarks in final states with at least one Z boson decaying into a pair of electrons or muons in pp collision data collected with the ATLAS detector at $\sqrt{s} = 13$ TeV*, *Phys. Rev.* **D98** (2018) 112010, [[1806.10555](#)].
- [9] ATLAS collaboration, M. Aaboud et al., *Search for pair production of up-type vector-like quarks and for four-top-quark events in final states with multiple b-jets with the ATLAS detector*, *JHEP* **07** (2018) 089, [[1803.09678](#)].
- [10] CMS collaboration, A. M. Sirunyan et al., *Search for vector-like quarks in events with two oppositely charged leptons and jets in proton-proton collisions at $\sqrt{s} = 13$ TeV*, *Eur. Phys. J.* **C79** (2019) 364, [[1812.09768](#)].
- [11] CMS collaboration, A. M. Sirunyan et al., *Search for top quark partners with charge 5/3 in the same-sign dilepton and single-lepton final states in proton-proton collisions at $\sqrt{s} = 13$ TeV*, *JHEP* **03** (2019) 082, [[1810.03188](#)].
- [12] CMS collaboration, A. M. Sirunyan et al., *Search for pair production of vector-like quarks in the $bW\bar{b}W$ channel from proton-proton collisions at $\sqrt{s} = 13$ TeV*, *Phys. Lett.* **B779** (2018) 82–106, [[1710.01539](#)].
- [13] CMS collaboration, A. M. Sirunyan et al., *Search for pair production of vector-like quarks in the fully hadronic final state*, [[1906.11903](#)].
- [14] J. Serra, *Beyond the Minimal Top Partner Decay*, *JHEP* **09** (2015) 176, [[1506.05110](#)].
- [15] A. Anandakrishnan, J. H. Collins, M. Farina, E. Kuflik and M. Perelstein, *Odd Top Partners at the LHC*, *Phys. Rev.* **D93** (2016) 075009, [[1506.05130](#)].

- [16] J. A. Aguilar-Saavedra, D. E. Lopez-Fogliani and C. Munoz, *Novel signatures for vector-like quarks*, *JHEP* **06** (2017) 095, [[1705.02526](#)].
- [17] M. Chala, *Direct bounds on heavy toplike quarks with standard and exotic decays*, *Phys. Rev.* **D96** (2017) 015028, [[1705.03013](#)].
- [18] H. Han, L. Huang, T. Ma, J. Shu, T. M. P. Tait and Y. Wu, *Six Top Messages of New Physics at the LHC*, [1812.11286](#).
- [19] S. Banerjee, M. Chala and M. Spannowsky, *Top quark FCNCs in extended Higgs sectors*, *Eur. Phys. J.* **C78** (2018) 683, [[1806.02836](#)].
- [20] J. H. Kim, S. D. Lane, H.-S. Lee, I. M. Lewis and M. Sullivan, *Searching for Dark Photons with Maverick Top Partners*, [1904.05893](#).
- [21] N. Bizot, G. Cacciapaglia and T. Flacke, *Common exotic decays of top partners*, *JHEP* **06** (2018) 065, [[1803.00021](#)].
- [22] G. C. Branco, P. M. Ferreira, L. Lavoura, M. N. Rebelo, M. Sher and J. P. Silva, *Theory and phenomenology of two-Higgs-doublet models*, *Phys. Rept.* **516** (2012) 1–102, [[1106.0034](#)].
- [23] M. Badziak, *Interpreting the 750 GeV diphoton excess in minimal extensions of Two-Higgs-Doublet models*, *Phys. Lett.* **B759** (2016) 464–470, [[1512.07497](#)].
- [24] A. Angelescu, A. Djouadi and G. Moreau, *Scenarii for interpretations of the LHC diphoton excess: two Higgs doublets and vector-like quarks and leptons*, *Phys. Lett.* **B756** (2016) 126–132, [[1512.04921](#)].
- [25] A. Arhrib, R. Benbrik, S. J. D. King, B. Manaut, S. Moretti and C. S. Un, *Phenomenology of 2HDM with vectorlike quarks*, *Phys. Rev.* **D97** (2018) 095015, [[1607.08517](#)].
- [26] S. De Curtis, L. Delle Rose, S. Moretti and K. Yagyu, *A Concrete Composite 2-Higgs Doublet Model*, *JHEP* **12** (2018) 051, [[1810.06465](#)].
- [27] S. Kanemura, T. Kubota and E. Takasugi, *Lee-Quigg-Thacker bounds for Higgs boson masses in a two doublet model*, *Phys. Lett.* **B313** (1993) 155–160, [[hep-ph/9303263](#)].
- [28] B. Gripaios, A. Pomarol, F. Riva and J. Serra, *Beyond the Minimal Composite Higgs Model*, *JHEP* **04** (2009) 070, [[0902.1483](#)].
- [29] J. Barnard, T. Gherghetta and T. S. Ray, *UV descriptions of composite Higgs models without elementary scalars*, *JHEP* **02** (2014) 002, [[1311.6562](#)].
- [30] G. Ferretti and D. Karateev, *Fermionic UV completions of Composite Higgs models*, *JHEP* **03** (2014) 077, [[1312.5330](#)].
- [31] A. Belyaev, G. Cacciapaglia, H. Cai, G. Ferretti, T. Flacke, A. Parolini et al., *Di-boson signatures as Standard Candles for Partial Compositeness*, *JHEP* **01** (2017) 094, [[1610.06591](#)]. [Erratum: *JHEP*12,088(2017)].
- [32] K. Agashe, R. Contino, L. Da Rold and A. Pomarol, *A Custodial symmetry for $Zb\bar{b}$* , *Phys. Lett.* **B641** (2006) 62–66, [[hep-ph/0605341](#)].
- [33] A. De Simone, O. Matsedonskyi, R. Rattazzi and A. Wulzer, *A First Top Partner Hunter’s Guide*, *JHEP* **04** (2013) 004, [[1211.5663](#)].
- [34] M. Bauer, M. Neubert and A. Thamm, *Collider Probes of Axion-Like Particles*, *JHEP* **12** (2017) 044, [[1708.00443](#)].
- [35] N. Craig, A. Hook and S. Kasko, *The Photophobic ALP*, *JHEP* **09** (2018) 028, [[1805.06538](#)].

- [36] ATLAS collaboration, M. Aaboud et al., *Search for new phenomena in high-mass diphoton final states using 37 fb^{-1} of proton–proton collisions collected at $\sqrt{s} = 13 \text{ TeV}$ with the ATLAS detector*, *Phys. Lett.* **B775** (2017) 105–125, [[1707.04147](#)].
- [37] CMS collaboration, A. M. Sirunyan et al., *Search for standard model production of four top quarks with same-sign and multilepton final states in proton-proton collisions at $\sqrt{s} = 13 \text{ TeV}$* , *Eur. Phys. J.* **C78** (2018) 140, [[1710.10614](#)].
- [38] J. Alwall, R. Frederix, S. Frixione, V. Hirschi, F. Maltoni, O. Mattelaer, H.S. Shao, T. Stelzer, P. Torrielli and M. Zaro, *The automated computation of tree-level and next-to-leading order differential cross sections, and their matching to parton shower simulations*, *JHEP* **07** (2014) 079, [[1405.0301](#)].
- [39] C. Degrande, C. Duhr, B. Fuks, D. Grellscheid, O. Mattelaer and T. Reiter, *UFO - The Universal FeynRules Output*, *Comput. Phys. Commun.* **183** (2012) 1201–1214, [[1108.2040](#)].
- [40] T. Sjostrand, S. Ask, J.R. Christiansen, R. Corke, N. Desai, P. Ilten, S. Mrenna, S. Prestel and C.O. Rasmussen, *An Introduction to PYTHIA 8.2*, *Computer Physics Communications* **191** (2014) 159–177, [[1410.3012](#)].
- [41] J. de Favereau, C. Delaere, A. Giammance, V. Lemaître, A. Mertens and M. Selvaggi, *DELPHES 3 A modular framework for fast simulation of a generic collider experiment*, *JHEP* **02** (2014) 057, [[1307.6346](#)].
- [42] NNPDF collaboration, R. D. Ball et al., *Parton distributions from high-precision collider data*, *Eur. Phys. J.* **C77** (2017) 663, [[1706.00428](#)].
- [43] A. Buckley, J. Ferrando, S. Lloyd, K. Nordström, B. Page, M. Rüfenacht et al., *LHAPDF6: parton density access in the LHC precision era*, *Eur. Phys. J.* **C75** (2015) 132, [[1412.7420](#)].
- [44] E. Conte, B. Fuks and G. Serret, *MadAnalysis 5, A User-Friendly Framework for Collider Phenomenology*, *Comput. Phys. Commun.* **184** (2013) 222–256, [[1206.1599](#)].
- [45] E. Conte and B. Fuks, *Confronting new physics theories to LHC data with MADANALYSIS 5*, *Int. J. Mod. Phys.* **A33** (2018) 1830027, [[1808.00480](#)].
- [46] M. Aliev, H. Lacker, U. Langenfeld, S. Moch, P. Uwer and M. Wiedermann, *HATHOR: HAdronic Top and Heavy quarks crOss section calculatoR*, *Comput. Phys. Commun.* **182** (2011) 1034–1046, [[1007.1327](#)].
- [47] ATLAS collaboration, M. Aaboud et al., *Measurement of the photon identification efficiencies with the ATLAS detector using LHC Run 2 data collected in 2015 and 2016*, *Eur. Phys. J.* **C79** (2019) 205, [[1810.05087](#)].
- [48] ATLAS Collaboration, *Electron efficiency measurements with the ATLAS detector using the 2015 LHC proton-proton collision data*, Tech. Rep. ATLAS-CONF-2016-024, CERN, Geneva, Jun, 2016.
- [49] M. Cacciari, G.P. Salam and G. Soyez, *FastJet user manual*, *European Physical Journal C* **72** (2012) , [[1111.6097](#)].
- [50] M. Cacciari, G. P. Salam and G. Soyez, *The anti- k_t jet clustering algorithm*, *JHEP* **04** (2008) 063, [[0802.1189](#)].
- [51] ATLAS Collaboration, *Expected performance of the ATLAS b-tagging algorithms in Run-2*, *ATL-PHYS-PUB-2015-022* (2015) .

- [52] A. D. Martin, W. J. Stirling, R. S. Thorne and G. Watt, *Parton distributions for the LHC*, *Eur. Phys. J.* **C63** (2009) 189–285, [0901.0002].
- [53] M. L. Mangano, M. Moretti, F. Piccinini and M. Treccani, *Matching matrix elements and shower evolution for top-quark production in hadronic collisions*, *JHEP* **01** (2007) 013, [hep-ph/0611129].
- [54] ATLAS collaboration, M. Aaboud et al., *Search for new phenomena in high-mass diphoton final states using 37 fb^{-1} of proton–proton collisions collected at $\sqrt{s} = 13\text{ TeV}$ with the ATLAS detector*, *Phys. Lett.* **B775** (2017) 105–125, [1707.04147]. auxiliary material Fig 1, <http://atlas.web.cern.ch/Atlas/GROUPS/PHYSICS/PAPERS/HIGG-2016-17/>.
- [55] T. P. Li and Y. Q. Ma, *Analysis methods for results in gamma-ray astronomy*, *Astrophys. J.* **272** (1983) 317–324.
- [56] R. D. Cousins, J. T. Linnemann and J. Tucker, *Evaluation of three methods for calculating statistical significance when incorporating a systematic uncertainty into a test of the background-only hypothesis for a Poisson process*, *Nucl. Instrum. Meth.* **A595** (2008) 480–501, [physics/0702156].
- [57] G. Cowan, K. Cranmer, E. Gross and O. Vitells, *Asymptotic formulae for likelihood-based tests of new physics*, *Eur. Phys. J.* **C71** (2011) 1554, [1007.1727]. [Erratum: *Eur. Phys. J.* C73,2501(2013)].
- [58] G. Cowan, “Some Statistical Tools for Particle Physics.” 2016.
- [59] ATLAS collaboration, M. Aaboud et al., *Searches for the $Z\gamma$ decay mode of the Higgs boson and for new high-mass resonances in pp collisions at $\sqrt{s} = 13\text{ TeV}$ with the ATLAS detector*, *JHEP* **10** (2017) 112, [1708.00212].
- [60] CMS collaboration, A. M. Sirunyan et al., *Search for $Z\gamma$ resonances using leptonic and hadronic final states in proton-proton collisions at $\sqrt{s} = 13\text{ TeV}$* , *JHEP* **09** (2018) 148, [1712.03143].
- [61] ATLAS collaboration, M. Aaboud et al., *Search for Higgs boson pair production in the $\gamma\gamma WW^*$ channel using pp collision data recorded at $\sqrt{s} = 13\text{ TeV}$ with the ATLAS detector*, *Eur. Phys. J.* **C78** (2018) 1007, [1807.08567].
- [62] ATLAS collaboration, M. Aaboud et al., *Search for Higgs boson pair production in the $\gamma\gamma b\bar{b}$ final state with 13 TeV pp collision data collected by the ATLAS experiment*, *JHEP* **11** (2018) 040, [1807.04873].
- [63] CMS collaboration, A. M. Sirunyan et al., *Search for physics beyond the standard model in high-mass diphoton events from proton-proton collisions at $\sqrt{s} = 13\text{ TeV}$* , *Phys. Rev.* **D98** (2018) 092001, [1809.00327].
- [64] D. Eriksson, J. Rathsman and O. Stål, *2HDMC: Two-Higgs-doublet model calculator*, *Comput. Phys. Commun.* **181** (2010) 833–834.
- [65] J. Horejsi and M. Kladiva, *Tree-unitarity bounds for THDM Higgs masses revisited*, *Eur. Phys. J.* **C46** (2006) 81–91, [hep-ph/0510154].
- [66] P. Bechtle, O. Brein, S. Heinemeyer, O. Stål, T. Stefaniak et al., *HiggsBounds – 4: Improved Tests of Extended Higgs Sectors against Exclusion Bounds from LEP, the Tevatron and the LHC*, *Eur. Phys. J.* **C74** (2014) 2693, [1311.0055].
- [67] P. Bechtle, S. Heinemeyer, O. Stål, T. Stefaniak and G. Weiglein, *HiggsSignals*:

Confronting arbitrary Higgs sectors with measurements at the Tevatron and the LHC, *Eur. Phys. J. C* **74** (2014) 2711, [[1305.1933](#)].

- [68] D. Buarque Franzosi, G. Cacciapaglia and A. Deandrea, *Sigma-assisted natural composite Higgs*, [1809.09146](#).
- [69] G. Belanger, R. M. Godbole, L. Hartgring and I. Niessen, *Top Polarization in Stop Production at the LHC*, *JHEP* **05** (2013) 167, [[1212.3526](#)].
- [70] D. Barducci and L. Panizzi, *Vector-like quarks coupling discrimination at the LHC and future hadron colliders*, *JHEP* **12** (2017) 057, [[1710.02325](#)].